Materials Advances

ROYAL SOCIETY OF CHEMISTRY

PAPER

View Article Online
View Journal

Cite this: DOI: 10.1039/d6ma00347h

Explainable machine learning-interpreted numerical analysis of $CsSnBr_3$ perovskite solar cells with diverse electron transport layers

M. Humayet Islam, [ab] Tanzir Ahamed, *[c] Md. Shihab Uddin, *[bd] M. Jalal Uddin, [a] M. M. Alam, *[a] Md. Ali Hossain,[b] Md Masum Billah,[b] Md. Hasanuzzaman Dipu[b] and Fernaz Narin Nur[b]

Among emerging photovoltaic technologies, perovskite solar cells (PSCs) are getting increasingly more research attention for being efficient and cheap. Using SCAPS-1D simulation software, this work uses $CsSnBr_3$ as the absorber material, which is placed between the electron transport layer (ETL) made up of $PC_{60}BM$, CdS, SnS_2, and CdZnS, and the hole transport layer (HTL). The thickness of the absorber and other factors like defect and doping densities are varied to indicate an optimized performance. The optimized configuration, $FTO/SnS_2/CsSnBr_3/MoO_3/Au$, demonstrates a power conversion efficiency (PCE) of 19.58% relative to alternative structures. Three additional structures have been optimized, and all four structures demonstrate ideal solar cell behavior, as confirmed by variations in series and shunt resistance, current–voltage (J–V), quantum efficiency (QE) characteristics, and generation and recombination rates. The structures exhibit optimal efficiency at room temperature. Additionally, a machine learning-assisted analysis has been employed to identify the device design parameters having the highest influence on the performance. Correlation mapping, regression modeling, and SHAP interpretability confirm that absorber doping, ETL donor density, and HTL acceptor density predominantly control the V_{OC}, J_{SC}, FF, and overall PCE. The integrated SCAPS-ML framework provides deeper physical insights and accelerates the optimization of $CsSnBr_3$-based perovskite solar cells.

Received 12th March 2026,
Accepted 13th April 2026

DOI: 10.1039/d6ma00347h

rsc.li/materials-advances

1. Introduction

The rising energy demand is leading to the swift depletion of conventional resources, which creates issues, such as contaminants in the environment and CO_2 emissions.[1–3] Perovskite solar cells (PSCs) have garnered considerable research interest for future solar cell technologies because of their remarkable optoelectronic characteristics.[4] These factors include a suitable bandgap, a significant absorption coefficient, minimal exciton binding energy, and efficient charge transportation for achieving power conversion efficiency (PCE) values exceeding 25%.[5–8] While lead (Pb)-based PSCs demonstrate superior efficiencies to Pb-free alternatives, the related toxic effects and sustainability issues present significant challenges.[9] In response to these issues, Pb-free perovskites have been promoted to support the advancements in performance.[9–11] In the past few years, there has been a notable surge in the performance of PSCs, with certain devices nearing or exceeding 30% efficiency for a single cell. However, one major barrier still exists: these advancements are mostly theoretical in nature.[12,13]

Among the alternatives to Pb, certain perovskite materials have surfaced as remarkable candidates for absorption, which is attributed to their exceptional electrical and optical characteristics.[14,15] Tin (Sn)-based perovskites show a lot of potential because they exhibit better optical and electrical characteristics, increased charge mobility, and smaller bandgaps.[16,17] Following this pathway, the generic perovskite material $CsSnBr_3$ demonstrates superior optoelectronic properties for use in PSCs. It is characterized by significant absorption in the visible light range and a small recombination rate, both essential for boosting the efficiency of solar cells.[18,19] The bandgap of a material is adjusted through external forces like hydrostatic stress, resulting in the manipulation of electrical and spectral properties.[20] For example, the addition of reduced graphene oxide (rGO) into $CsSnBr_3$ has been reported to improve structural and optical characteristics. The

[a] Department of Electrical and Electronic Engineering, Islamic University, Kushtia-7003, Bangladesh. E-mail: malam@eee.iu.ac.bd
[b] Department of Computer Science and Engineering, Daffodil International University, Dhaka-1216, Bangladesh. E-mail: su130776@gmail.com
[c] Department of Electrical and Electronic Engineering, CCN University of Science and Technology, Cumilla-3503, Bangladesh. E-mail: tanzir.eee2k15@gmail.com
[d] NanoBio Technology Center, Daffodil International University, Dhaka-1216, Bangladesh

incorporation of rGO enhances the photon absorption, surface roughness, and crystalline quality of the main absorber, which affords an improvement in the power conversion efficiency of 5.27% for the optimized devices.[21,22] A conjugation method at room temperature utilizing ethanol and acidic ingredients has demonstrated the ability to yield extremely durable cubic-phase $CsSnBr_3$ perovskites.[23] Dar *et al.* conducted a numerical investigation of $CsSnBr_3$ utilizing SCAPS-1D software. They integrated various conventional electron transport layers (ETLs) and hole transport layers (HTLs) to demonstrate the superiority of this material in attaining a maximum power conversion efficiency (PCE) of 20.02% in the configuration ITO/WS_2/$CsSnBr_3$/Cu_2O/Au.[24] Kheswa *et al.* investigated materials using ZnO as the ETL and reduced graphene oxide (rGO) as the HTL, achieving an overall efficiency of 26.92%.[25] The bilayer structure $MAPbI_3$/$CsSnBr_3$ was investigated to improve its performance by extending spectral coverage and minimizing heating effects, which attained a peak PCE of 29.87%.[26] In terms of experimental studies, the research study conducted by Fang *et al.* achieved a PCE of 1.5% using the FTO/TiO_2/$CsSnBr_3$/MoO_3/Al configuration of PSCs.[27] Furthermore, Gupta and colleagues investigated a solar cell made of $CsSnBr_3$ and found that the FTO/TiO_2/$CsSnBr_3$/spiro-OMeTAD/Au configuration exhibited the highest PCE of 2.1%.[28] An exceptionally elevated efficiency was further observed by another experimental study carried out by Chen *et al.* on ITO/TiO_2/$CsSnBr_3$/Spiro-OMeTAD/Au.[29] Therefore, there are other carrier transport materials that are yet to be considered when combining $CsSnBr_3$ absorber materials. Based on these studies, more carrier transport materials have yet to be studied for integration with the $CsSnBr_3$ absorber material. Perovskite materials have a wide variety of crystal structures that can greatly determine their optoelectronic characteristics and device behaviour. The standard perovskite has the formula ABX_3, with A, B, and X representing a monovalent cation, a divalent metal cation, and a halide anion, forming a three-dimensional set of corner-sharing BX_6 octahedra.[30] This design has been extensively studied because it has a high carrier mobility, a tunable bandgap, and excellent light absorption. In addition to this classical geometry, other perovskite-derived geometries, including A_3BX_3 and $A_2BB'X_6$ double perovskites, have also recently been of interest. Specifically, $A_2BB'X_6$ with two distinct metal cations at the B-site is promising as it is more stable in the environment and less toxic than Pb-based equivalents, which are more toxic and less stable.[31] Also, variants with vacancy orders and low-dimensional perovskites have been explored to enhance moisture resistance and structural stability, but they usually have worse carrier transport properties. Recent advancements in perovskite solar cells have focused on improving their efficiency, stability, and environmental compatibility, with reported efficiencies near or more than 30% in tandem configurations and continuous progress in lead-free materials.[32] In this context, Sn-based ABX_3 perovskites such as $CsSnBr_3$ have emerged as promising alternatives due to their suitable bandgap, high absorption coefficient, and structural similarity to Pb-based perovskites, achieving competitive photovoltaic performance while mitigating toxicity concerns.[33] Despite these advancements, systematic studies integrating advanced simulation and data-driven approaches for optimizing Pb-free $CsSnBr_3$-based devices remain limited.

PSCs usually have an absorber layer between an ETL and an HTL to get the most out of them.[34] Usually, the ETL and HTL are made from n-type and p-type materials, respectively, with the help of a doping mechanism. When the photon energy from light hits the HTL, it makes it easier to get holes out, and when light hits the ETL, it gets the photoelectrons out of the absorber material.[35] Due to their outstanding electrical characteristics, strong chemical stability, superior processability, and versatility, titanium dioxide (TiO_2) and 2,2′,7,7′-tetrakis[*N*,*N*-di(4-methoxyphenyl)amino]-9,9′-spirobifluorene (Spiro-OMeTAD) are predominantly utilized as the electron transport layer and hole transport layer, respectively, for PSCs.[36–39] However, the addition of CdS improves energy level alignment and facilitates efficient charge transport from the perovskite layer to the ETL, resulting in efficiencies exceeding 15%.[40] A study by Khan *et al.* investigated CdZnS as an ETL within the CMTS/$CsGeI_3$/CdZnS structure, achieving a peak PCE of 25.78%.[41] Other ETL materials like SnS_2 have been utilized in Pb-free perovskite solar cells, achieving PCEs of 29.75% and 33.61% with different absorber materials, showcasing their versatility.[42] In the same line, Xie *et al.* reported that PCBM can be used as an ETL in PSCs, showing improved efficiency with a PCE advancement to 19.31%.[43] However, there remains a notable lack of integrated SCAPS-machine learning (ML) frameworks specifically tailored for Pb-free $CsSnBr_3$ PSCs, highlighting a critical research gap that this study aims to address.

This work presents a comprehensive comparative analysis of multiple electron transport layers ($PC_{60}BM$, CdS, SnS_2, and CdZnS) in Pb-free $CsSnBr_3$ PSCs, combined with an integrated machine learning framework enhanced by SHAP-based interpretability. Additionally, the thicknesses, doping densities, and defect densities of various layers have been systematically varied to identify the optimal structures. The influences of resistance and temperature, quantum efficiencies, and current–voltage curves have been examined for the optimized structures to sum up the total package.

2. Materials and methodology

2.1. $CsSnBr_3$-based PSC structures

The initial structure was made with the standard n–i–p configuration of the PSC. This study involved the effective application of fluorine-doped tin oxide (FTO) as the front contact material in the simulation work. In the primary configuration, $CsSnBr_3$ served as the absorber layer, while $PC_{60}BM$, CdS, SnS_2, and CdZnS were utilized as ETLs. MoO_3 functioned as the HTL, and Au was employed as the back metal contact (BMC). Initially, the FTO substrate underwent a cleaning process to eliminate any surface contaminants, after which the ETL ($PC_{60}BM$, CdS, SnS_2, and CdZnS) was deposited onto the FTO.[44] After the ETL deposition, a vacuum evaporation method was used to grow a

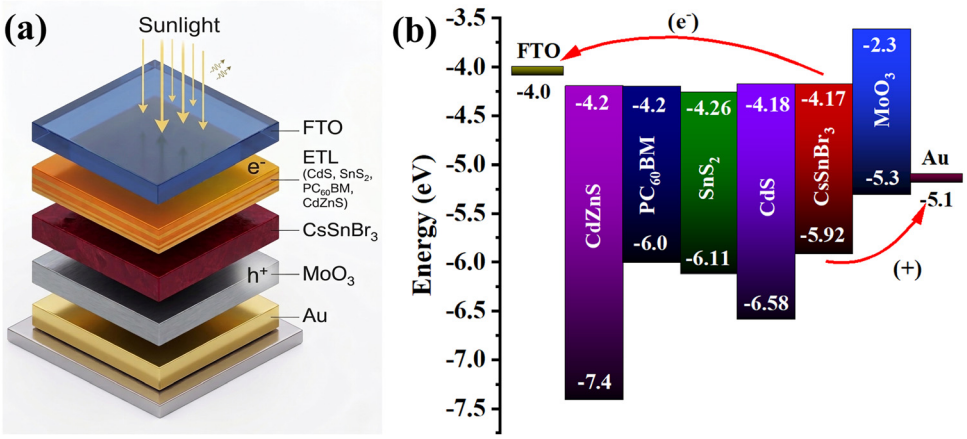

Fig. 1 (a) PSC structure with the suggested materials. (b) Energy band alignment of the absorber material with other materials.

Table 1 Initial numerical data for the FTO, absorber, ETL, and HTL

Material property	FTO	CdZnS	$PC_{60}BM$	SnS_2	CdS	$CsSnBr_3$	MoO_3
Thickness (nm)	200	100	50	150	50	500	100
Bandgap, E_g (eV)	3.5	3.2	1.8	1.85	2.4	1.75	3.0
Electron affinity, χ (eV)	4	4.2	4.2	4.26	4.18	4.17	2.3
Relative dielectric permittivity, ε_r	9	9.12	4	17.7	10	9.93	18
Conduction band effective density of states, N_C (cm^{-3})	2.2×10^{18}	$1.5 \times 1\ 0^{18}$	1×10^{21}	7.32×10^{18}	2.2×10^{18}	1×10^{19}	1×10^{19}
Valence band effective density of states, N_V (cm^{-3})	1.8×10^{19}	1.8×10^{18}	2×10^{20}	1×10^{19}	1.9×10^{19}	1×10^{18}	2.2×10^{18}
Electron thermal velocity (cm s^{-1})	10^7	10^7	10^7	10^7	10^7	10^7	10^7
Hole thermal velocity (cm s^{-1})	10^7	10^7	10^7	10^7	10^7	10^7	10^7
Electron mobility, μ_n (cm^2 V^{-1} s^{-1})	20	250	0.1	50	100	15	210
Hole mobility, μ_h (cm^2 V^{-1} s^{-1})	10	40	0.1	25	25	5.85	210
Donor density, N_D (cm^{-3})	1×10^{18}	1×10^{16}	1×10^{17}	9.85×10^{19}	1×10^{18}	0	0
Acceptor density, N_A (cm^{-3})	0	0	0	0	0	1×10^{18}	1×10^{18}
Total density, N_t (cm^{-3})	1×10^{15}	1×10^{14}	1×10^{15}	1×10^{14}	1×10^{15}	1×10^{15}	1×10^{15}
References	48	49	50	51	51	52–54	55

thin layer of the $CsSnBr_3$ absorber.[45] Again, a thin coating of MoO_3 was made on the FTO substrate using a chemical bath deposition (CBD) process for epitaxial growth.[46] Using thermal evaporation, a thin coating of Au was placed on top of the HTL layer. This worked as the anode contact for collecting electrons from the ETL layer and sending them to the load side.[47] Fig. 1(a) presents a visual schematic of the simulated structures with FTO/($PC_{60}BM$, CdS, SnS_2, and CdZnS)/$CsSnBr_3$/MoO_3/Au configurations. The PSC structure is also presented through four distinct layers as ETLs in the energy band alignment diagram in Fig. 1(b). From the diagram, it is clear that the carriers have a smooth path to travel to reach their corresponding electrode. The simulation with SCAPS-1D was conducted using the input parameters outlined in Table 1. The initially defined conditions for this study are listed in Table 2. We used a density of interfacial defects of 10^{10} cm^{-2} at the ETL/absorber interface and absorber/HTL interface. This is a common supposition applied in SCAPS-1D modelling to assess the top-level performance of solar cell structures under reduced recombination losses. Nevertheless, in real-world equipment, interfacial defect densities may differ by many orders of magnitude due to fabrication conditions and material quality. An increase in the defect density at the interface will generally add more recombination centres, which will result in a decreased open-circuit voltage and efficiency. Hence, although a predetermined low figure is applied for the analysis of the baseline, the potential impact on the performance of the equipment is seriously recognized in the given work.

2.2. Energy band diagram of PSC structures

The alignment of energy bands in each material is essential for optimal carrier transmission. The carrier transport layer, including the ETL and HTL, pushes the movement of carriers to their designated electrodes. The ETL enables the transfer of electrons while contemporaneously blocking holes. By contrast, the HTL enhances hole mobility but lowers the flow of

Table 2 Boundary conditions and initial simulation parameters used in the SCAPS-1D framework

Parameter	Value
Temperature	300 K
Illumination	AM 1.5 G and 1000 W m^{-2}
Series resistance (R_s)	0 Ω cm^2
Shunt resistance (R_{sh})	∞ Ω cm^2
Front contact work function	4.4 eV
Back contact work function	5.1 eV (Au)
Interface defect density	10^{10} cm^{-2}
Simulation mode	Illumination

electrons. A spike-like alignment occurs when the conduction band minimum of the ETL is slightly higher than that of the absorber, creating a small potential barrier. This barrier helps suppress the back-transfer of electrons and reduces interfacial recombination, thereby improving device performance when the spike is within the optimal range (~0–0.2 eV). Conversely, a cliff-like alignment is formed when the conduction band of the ETL is lower than that of the absorber, which eliminates the barrier but may lead to charge accumulation and enhanced recombination at the interface.[56,57] Fig. 2(a)–(d) depicts the energy band alignment for the proposed configurations of FTO/ETL/$CsSnBr_3$/MoO_3/Au, incorporating $PC_{60}BM$, CdS, SnS_2, and CdZnS as the electron transport layers. The electron affinity of the corresponding ETL must be greater than that of the absorber layer, whereas the electron affinity of the HTL should be lower than that of the absorber layer to facilitate the effective transfer of electrons and holes.[4] Favorable band alignment is maintained by all the materials in the proposed constructions, allowing the carriers to flow freely. This study employed highly efficient and proven carrier transport layers in consideration of the band alignment of the structures.

2.3. SCAPS-1D simulation software

Simulation tools are widely popular in the scientific community for their diversified applications to enhance the performance of solar devices.[58] Different simulation programs, like SILVACO ATLAS, AMPS, COMSOL, and SCAPS-1D, are used to study how well solar cells work as photovoltaic (PV) devices. SCAPS-1D is widely utilized and more popular due to its ability to accommodate seven distinct levels.[34,59] This layer comprises a heterostructure system that is facile to utilize and regulate in both light and dark environments. Professor M. Burgelman's software SCAPS-1D primarily relies on three fundamental equations: hole continuity, Poisson, and electron continuity equations mathematically from eqn (1)–(5).

The Poisson equation is given below:

$$-\frac{\partial}{\partial x}\left(-\varepsilon(x)\frac{\partial V}{\partial x}\right) = q[p(x) - n(x) + N_D{}^{+}(x) - N_A{}^{-}(x) + p_t(x) - n_t(x)]. \quad (1)$$

In this case, ε represents the dielectric permittivity, q represents the charge density, $N_A{}^{-}$ and $N_D{}^{+}$ represent the acceptor and donor densities, respectively, V represents the voltage, and p_t and n_t represent the densities of holes and electrons, respectively.

The continuity equations for the holes and electrons are given below:

$$\frac{\partial p}{\partial x} = \frac{1}{q}\frac{\partial J_p}{\partial x} + G_p - R_p \quad (2)$$

$$\frac{\partial n}{\partial x} = \frac{1}{q}\frac{\partial J_n}{\partial x} + G_n - R_n \quad (3)$$

Here, J_p and J_n are the hole and electron current densities, respectively, G_p and G_n are the generation of a hole and an

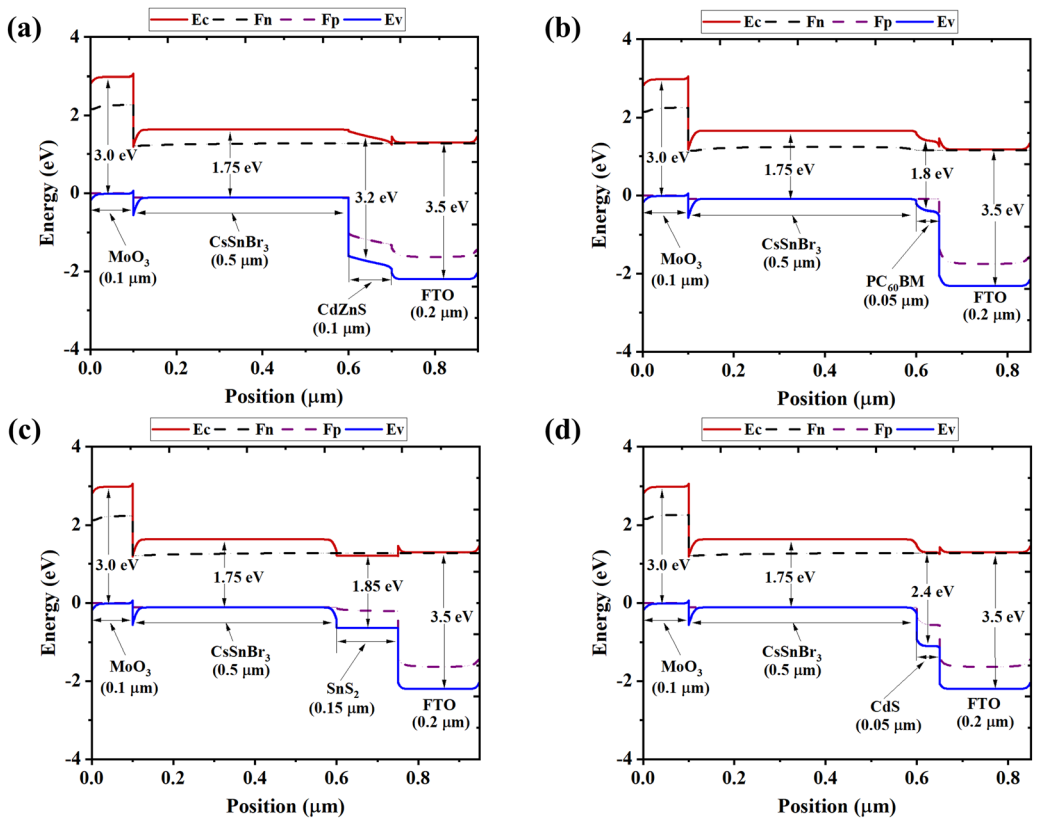

Fig. 2 Energy band diagrams of the $CsSnBr_3$-based perovskite solar cells with the configurations of (a) CdZnS, (b)$PC_{60}BM$, (c) SnS_2, and (d) CdS.

electron, respectively, and R_p and R_n are the recombination rates of the hole and electron, respectively.

The movement of charge carriers, specifically holes and electrons, within semiconductors can be described by the following constitutive relationships:

$$J_n = qn\mu_n\varepsilon + qD_n\partial n, \quad (4)$$

$$J_p = qp\mu_p\varepsilon + qD_p\partial p. \quad (5)$$

In this context, μ_p represents the hole mobility, while μ_n indicates the electron mobility. D_n, D_p, and ε are the diffusion coefficients of the electron, hole, and electric field, respectively. ∂n and ∂p are the gradients for electron and hole concentrations, respectively.

The material absorption model was chosen as the square root of $(h\nu - E_g)$, which is a built-in model in the software background. The main formula behind this procedure is the Tauc law. The main significance of this law is its straightforward techniques to determine the amorphous and disordered semiconductors' absorption pattern.[60] Eqn (6)–(8) show the mathematical modelling of this formula as follows:

$$\alpha(h\nu) = \left(\alpha_o + \beta_o\frac{E_g}{h\nu}\right)\sqrt{\frac{h\nu}{E_g} - 1}, \quad (6)$$

$$\alpha_o = A\sqrt{E_g}, \quad (7)$$

$$\beta_o = \sqrt{\frac{B}{E_g}}. \quad (8)$$

Here, α_o, β_o, E_g, h, and ν are the model constants, bandgap, Planck constant, frequency of the incident photons, respectively.

2.4. Machine learning-assisted evaluation and analysis

Recent developments in perovskite solar cell (PSC) research have demonstrated that numerical simulations alone often have a limited scope for understanding the complex patterns of structural, electrical, and optical parameters that govern device performance.[59] Numerical tools like SCAPS-1D can model device physics accurately, but exploring high-dimensional parameter spaces becomes computationally intensive for determination. It does not readily reveal nonlinear dependencies among variables in most of the simulations. To overcome these limitations, machine learning (ML) algorithms have been successfully integrated for Pb-free perovskites to accelerate the process of optimization, identify dominant features, and interpret degradation factors.[61,62] Motivated by these advancements in the literature, the present work incorporates ML-driven regression tools to comprehensively evaluate the performance of $CsSnBr_3$-based PSCs and identify the most influential physical parameters. The choice of machine learning models in this paper was informed by the objective to balance predictive accuracy, interpretability, and computational efficiency. Linear regression and multiple linear regression were used to assess the linear relationship between the parameters of the equipment and the photovoltaic outputs. These models are very interpretable but restricted in their ability to capture nonlinear interactions. Ensemble-based models (random forest and XGBoost) were introduced to resolve this weakness, as they are highly effective in capturing nonlinear relationships and the interaction of features. The techniques find application in material and device optimization problems, in which several interdependent physical parameters are involved in determining performance. Moreover, their resilience to noise and capacity to work with relatively small data sets render them suitable for the SCAPS-generated data. A dataset was generated by systematically varying the absorber doping concentration (N_A), absorber defect density (N_t), ETL donor concentration (N_D), HTL acceptor density (N_A), and absorber thickness in SCAPS-1D simulations. For each parameter combination, key PV output metrics, including open-circuit voltage (V_{OC}), short-circuit current density (J_{SC}), fill factor (FF), and power conversion efficiency (PCE), were recorded. The dataset was divided into training and testing sets using an 80 : 20 ratio, and model performance was further validated using a k = 5-fold cross-validation to ensure robustness and generalization. Four widely used regression models were implemented to predict these PV performance parameters: linear regression, multiple linear regression (MLP), random forest regressor, and XGBoost regressor. The purpose of this comparative modelling was to assess the predictive accuracy of different ML algorithms and determine which model most effectively captured the nonlinear device physics inherent in $CsSnBr_3$-based PSCs. SHapley Additive exPlanations (SHAP) analysis was employed to further interpret the contribution of each feature and reveal physically meaningful relationships between device parameters and PV performance.

3. Results and discussion

3.1. Effect of the thickness of the ETL and HTL on the efficiency of the PSCs

The primary objective of the ETL is to extract electrons from the absorber surface while preventing the recombination of holes. Fig. 3(a)–(d) shows how the PCE of the solar cell structure changes when the ETL and HTL thicknesses are varied. The thicknesses of the HTL and ETL were varied from 50 nm to 250 nm and from 30 nm to 200 nm, respectively. The PCE of the FTO/CdZnS/$CsSnBr_3$/MoO_3/Au structure increases from 14.1% to 14.3%. For the FTO/$PC_{60}BM$/$CsSnBr_3$/MoO_3/Au structure, the PCE increases from 12.7% to 13.67%. In the case of the FTO/SnS_2/$CsSnBr_3$/MoO_3/Au structure, the PCE improves from 14.98% to 16.53%. Lastly, for the FTO/CdS/$CsSnBr_3$/MoO_3/Au structure, the PCE increases from 14.48% to 15.27%. These findings demonstrate that there are only slight differences in the PCE across various thickness combinations of the HTL and ETL layers. The PCE is not very sensitive to an increase in the layer thickness, although small changes in the efficiency are observed. This means that the thickness variations of the ETL and HTL do not have a huge impact on the overall efficiency of

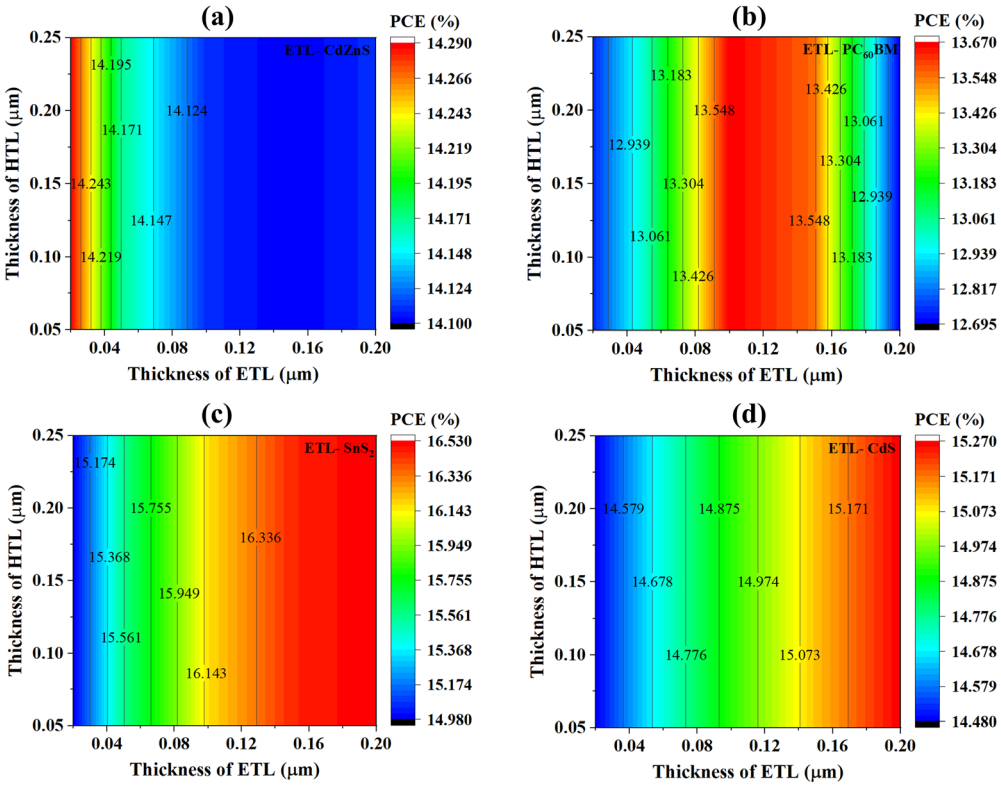

Fig. 3 Effect of changes in the ETL and HTL thicknesses on the efficiency of the solar cell structures of (a) CdZnS, (b) $PC_{60}BM$, (c) SnS_2, and (d) CdS.

the system with respect to the materials being investigated. This is why those parameters are not included in the main optimization of the device structures.[63]

3.2. Effect of the acceptor and defect densities of the absorber on the efficiency

The acceptor density of the absorber facilitates the splitting of charge carriers upon exposure to light.[4,64] Conversely, a high level of defects tends to increase recombination centres, where electrons and holes recombine, thereby hindering the generation of useful electrical current.[65,66] Fig. 4(a)–(d) demonstrates the effect of variations in the acceptor density (N_A) and defect density (N_t) of the absorber on the PCE of the solar cell architectures. The values of N_A and N_t were varied from 10^{17} cm^{-3} to 10^{20} cm^{-3} and from 10^{12} cm^{-3} to 10^{15} cm^{-3}, respectively. All structures exhibit increased efficiency at lower acceptor densities, with the exception of the configuration using SnS_2 as the electron transport layer. When SnS_2 serves as the electron transport layer, the device demonstrates a different pattern within the defect density upto 10^{15} cm^{-3}. Other devices do not highly appear to depend on a change in the N_t of the absorber. The decreased reliance on the N_t may be attributed to the inherent defect tolerance of the absorber material.

3.3. Effect of the donor and defect densities of the ETL on the efficiency

The donor density (N_D) refers to the concentration of donor atoms or molecules in a material that contributes to the generation of free electrons and enhances the electron mobility within the layer.[56] A high donor density typically improves electron transport, which may lead to enhanced and efficient charge collection.[58] This phenomenon leads to a better PCE of the simulated structures. Fig. 5(a)–(d) illustrates the alterations in the PCE corresponding to changes in the donor and defect densities of the ETL. The N_D and N_t of the ETL were varied from 10^{16} cm^{-3} to 10^{20} cm^{-3} and from 10^{12} cm^{-3} to 10^{16} cm^{-3}, respectively, to examine their impact on device performance. CdZnS and CdS exhibit similar behaviour, with the peak PCE observed after an N_D of 10^{19} cm^{-3}. This result demonstrates independence from variations in the defect density. The optimal efficiency of the structures comprising $PC_{60}BM$ and SnS_2 is observed at an N_t carrier concentration of less than 10^{14} cm^{-3}, showing minimal dependence on the donor density of the ETL.

3.3. Effect of the acceptor and defect densities of the HTL on the efficiency

Fig. 6(a)–(d) illustrates the variation in the acceptor and defect densities of the HTL, with the N_A ranging from 10^{16} cm^{-3} to 10^{20} cm^{-3} and the N_t varying from 10^{12} cm^{-3} to 10^{16} cm^{-3}, in order to assess their impact on the efficiency of the PSCs. Our findings indicate that an increase in the N_A of the HTL correlates with an improvement in the PCE. A greater PCE is achieved, particularly when the N_t is maintained within an optimal range. Among the materials evaluated, SnS_2 exhibits the highest overall efficiency of 17.33%, which results in elevated PCE values and is attributed to its wider range of

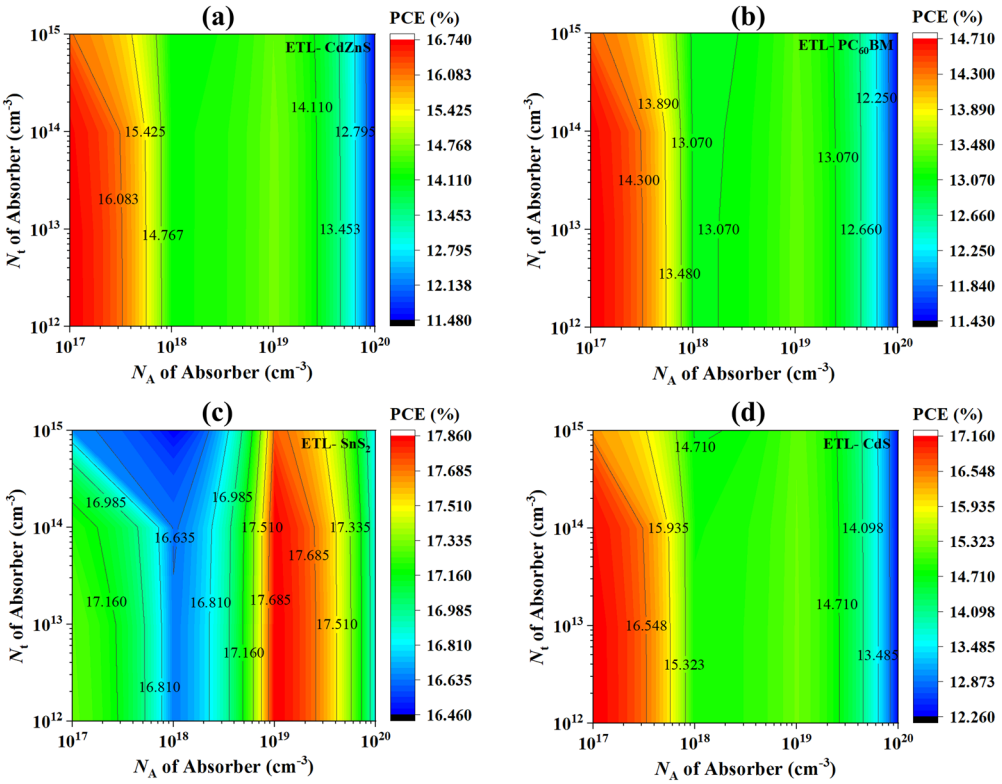

Fig. 4 Effect of changes in the acceptor and defect densities of the absorber on the efficiency of the solar cell structures of (a) CdZnS, (b) $PC_{60}BM$, (c) SnS_2, and (d) CdS.

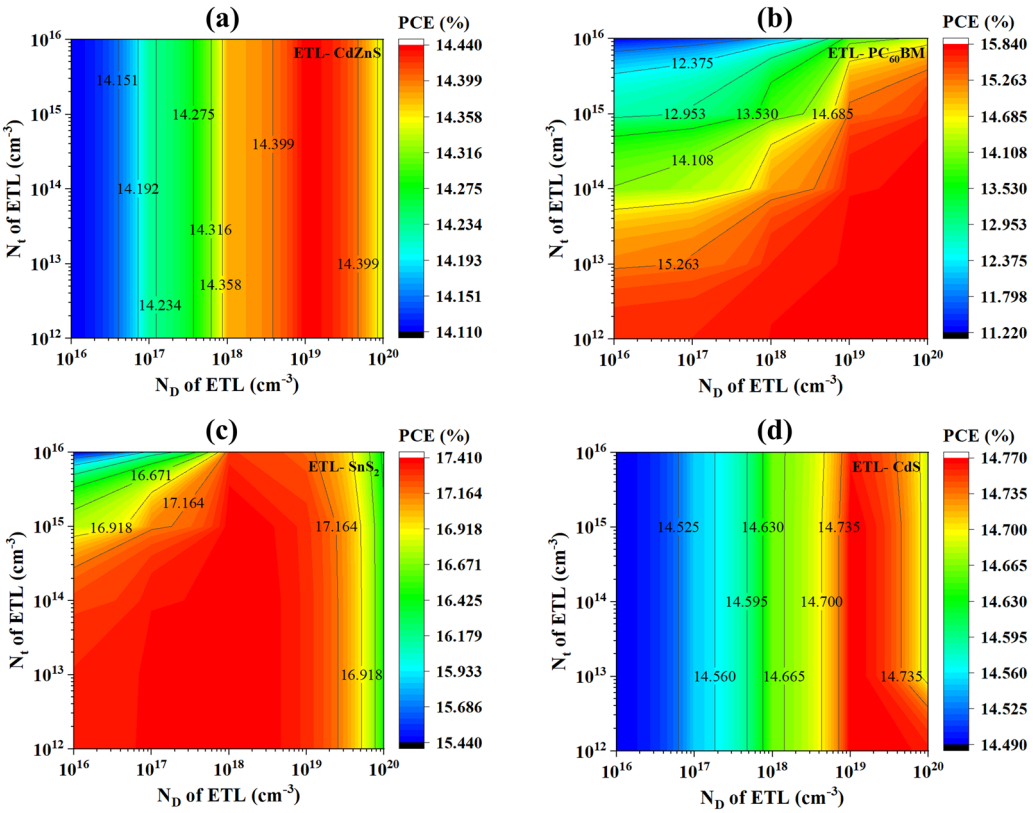

Fig. 5 Effect of changes in the donor and defect densities of the ETL on the efficiency of the solar cell structures of (a) CdZnS, (b) $PC_{60}BM$, (c) SnS_2, and (d) CdS.

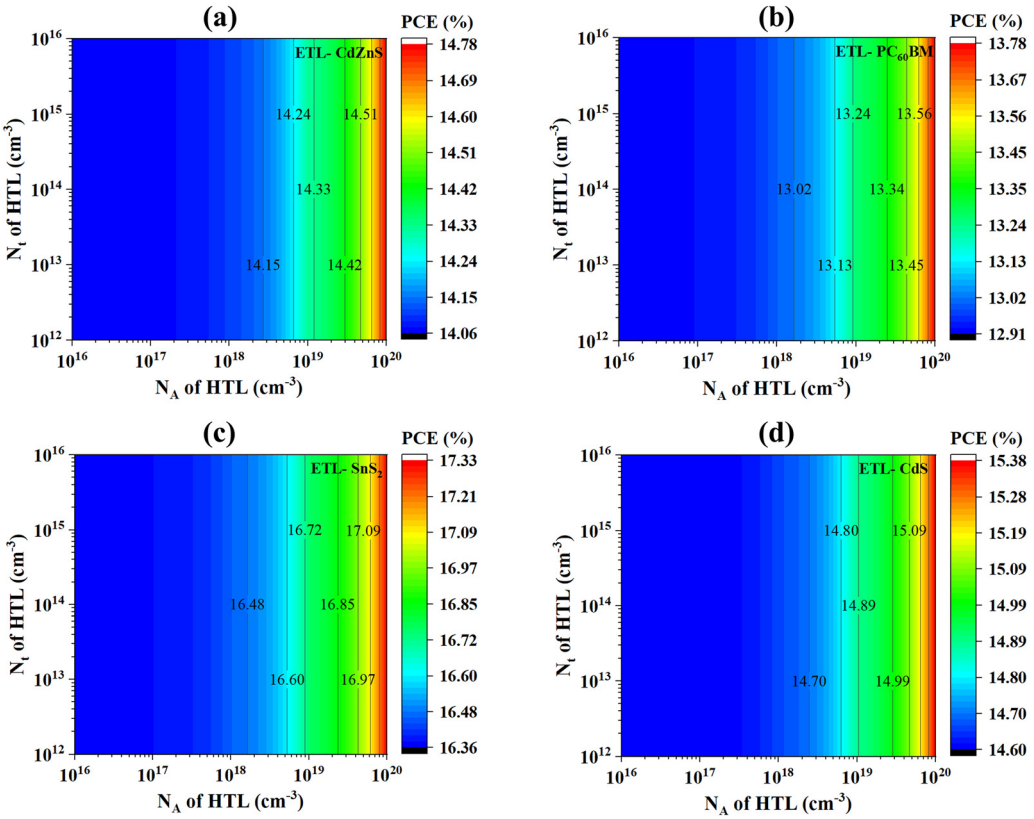

Fig. 6 Effect of changes in the acceptor and defect densities of the HTL on the efficiency of the solar cell structures of (a) CdZnS, (b) $PC_{60}BM$, (c) SnS_2, and (d) CdS.

defect and acceptor densities. All structures exhibit a consistent phenomenon of achieving higher PCEs at elevated values of the HTL N_A and are not influenced by the changes in the N_t of the HTL. This finding justifies the exclusion of specific parameter ranges from the structural optimization process to ensure accurate and reliable performance analysis.

Optimization of the absorber thickness

The absorber layer thickness is an important parameter of PSCs because it directly affects light absorption, carrier generation, and recombination dynamics.[64] In this study, the J_{SC} and PCE are found to rise with increasing absorber thickness to 1500 nm. The trend is largely explained by the ability of photons to be better absorbed and more electron–hole pairs to be generated at the higher thicknesses. A thicker absorber layer absorbs more light, which may increase the photocurrent.[64,67] However, if the thickness surpasses the diffusion length of the charge carriers, it may result in elevated recombination losses, as the carriers may not reach the electrodes within the required timeframe.[4] Additionally, thicker layers contribute to an increased optical path length and absorption. However, they also result in higher series resistance, which may lead to a decrease in the voltage and overall efficiency.[68] Fig. 7(a)–(d) illustrates the variations in the V_{OC}, J_{SC}, FF, and PCE as a function of the absorber layer thickness. The absorber layer thickness was varied from 800 nm to 1500 nm to assess its impact on performance parameters. All proposed structures exhibit a similar trend across the four performance parameters. The V_{OC} and FF exhibit a nearly constant curve. However, the J_{SC} and PCE values increase with the thickness of the layer. The trend matches the result from a previous study.[69] Given the expense and production abilities, the optimal thickness of the absorber layer is established to be 1500 nm for all four configurations.

3.4. Effect of the series resistance and shunt resistance

Both series (R_S) and shunt resistance (R_{Sh}) have a remarkable effect on the device performance because they control the gradients and contours of the current–voltage curves'. The defects in the material, especially those arising during production, along with back contact, may contribute to series and shunt resistances. The relation between the current density and these resistances can be understood from eqn (9).

$$J = J_L - J_0\left[\exp\left(\frac{e(V + JR_S)}{AK_BT}\right) - 1\right] - \frac{V + JR_S}{R_{Sh}} \quad (9)$$

In this case, J_JJ_L and J_0 are the short-circuit, induced and reverse saturation currents, respectively, e is the electric change, V is the voltage, K_B is the Boltzmann constant, T is the temperature, and R_{Sh} is the shunt resistance.

The impact of the series and shunt resistance on the power conversion efficacy was examined by concurrently varying these resistances, and the findings are shown in Fig. 8(a)–(d). The series resistance was varied from 1 Ω cm^2 to 6 Ω cm^2, while the

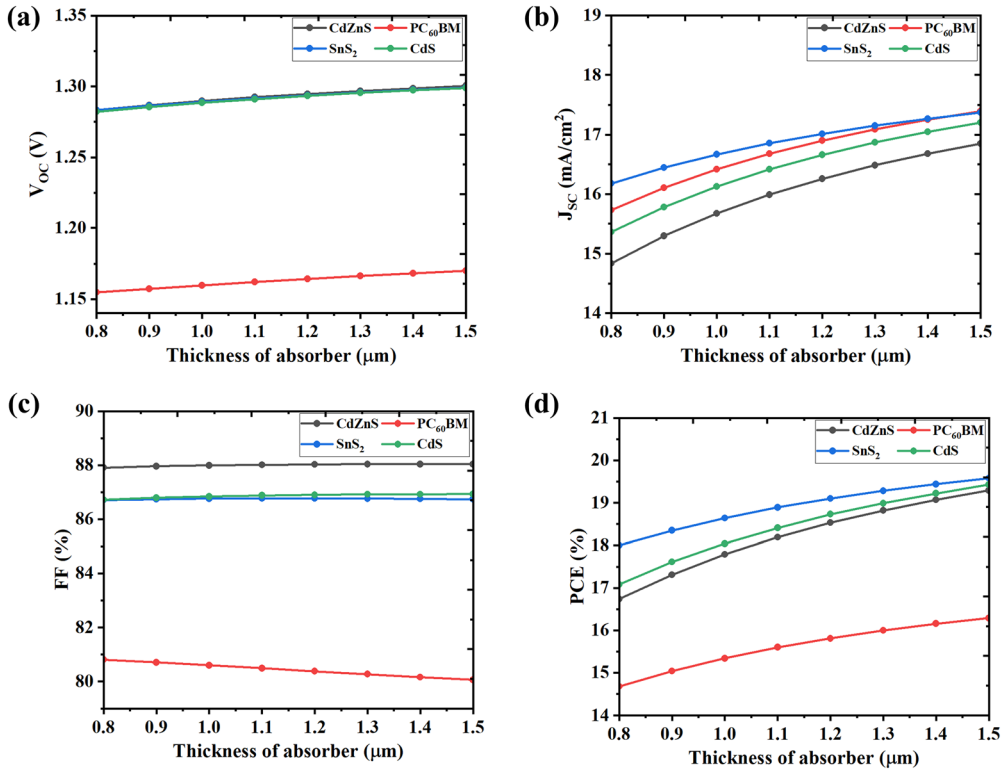

Fig. 7 Variation of the performance parameters, (a) V_{OC}, (b) J_{SC}, (c) FF, and (d) PCE, with the absorber layer thickness.

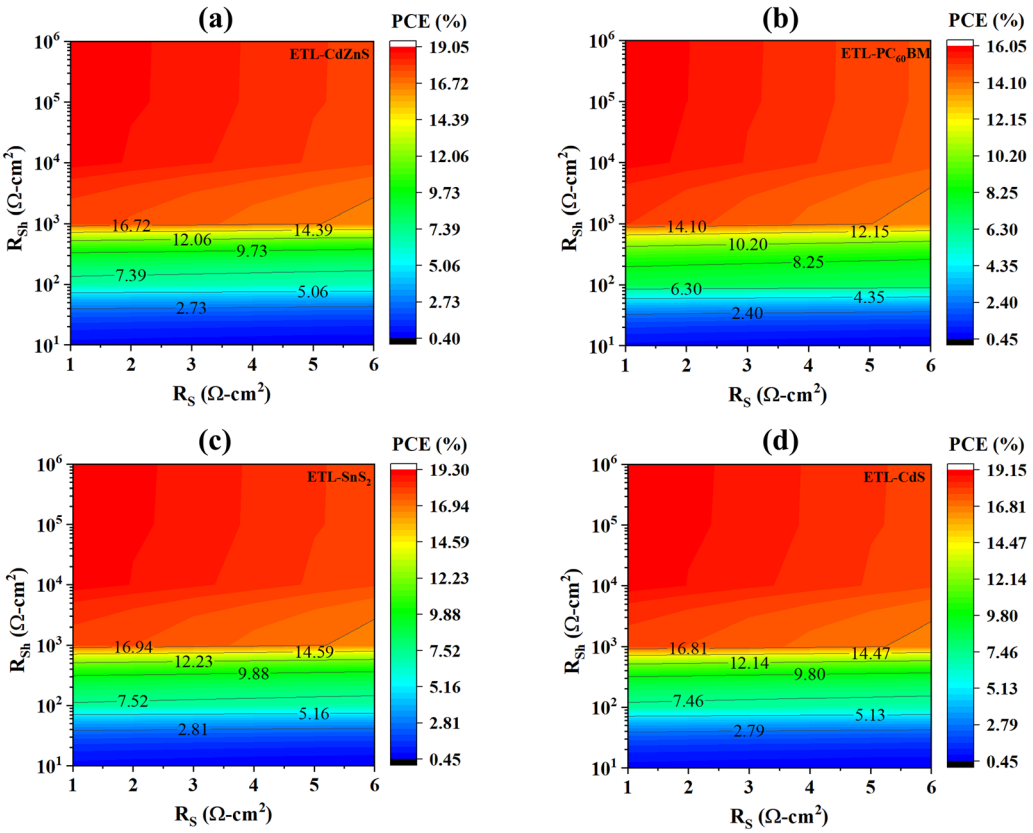

Fig. 8 Effect of the series and shunt resistances on the efficiency of the suggested solar cell structures of (a) CdZnS, (b) $PC_{60}BM$, (c) SnS_2, and (d) CdS.

shunt resistance was varied from 10 Ω cm^2 to 10^6 Ω cm^2. Based on the figures, lower series resistance and higher shunt resistance correlate with increased efficiency in the structures studied. For all four structures, when R_{Sh} surpasses 10^3 Ω cm^2, the PCE remains constant. Once R_{Sh} reaches a specific threshold, generally determined by the fundamental features of the device and materials, a further increase in R_{Sh} has yield negligible effects on efficiency. Increased series resistance results in less power supply to the device, leading to a decline in performance.

3.7. Impact of the temperature on performance metrics

Light is the primary component for the functioning of the solar cell, and it needs to be consistently positioned in a proper place to receive sunlight. This results in the temperature (T) of the solar cells being higher than the temperature of the surrounding environment. The influence of the temperature on the solar cell performance was examined by varying the operating temperature from 300 K to 450 K. Fig. 9(a)–(d) illustrates the alterations in the V_{OC}, J_{SC}, FF, and PCE as a function of temperature fluctuation. As the temperature increases, it induces reverse saturation current (J_0), which primarily contributes to a reduction in V_{OC} due to their inverse relationship, as illustrated by the following eqn (10):

$$V_{OC} = \frac{AK_BT}{q}\left[\ln\left(1+\frac{J_{SC}}{J_0}\right)\right], \quad (10)$$

where A is the ideality factor and $\frac{K_BT}{q}$ is the thermal voltage.

The values of the FF and PCE decline as the temperature rises, which can be attributed to the reduction in shunt resistance. The R_{Sh} decrease mainly occurs due to the increase in leakage current inside the cell. A reason for the reduction in the PCE may be the increased charge recombination rate at higher temperatures, which stems from a decline in charge recombination resistance.

3.8. *J–V* and QE characteristics curve

The short-circuit current density (J_{SC}) represents the highest possible current produced by a solar cell pursuant to light, while the open circuit voltage indicates the highest potential disparities achievable by the device, which is affected by the inherent electrical field and recombination losses within the cell.[59] Fig. 10(a) depicts the correlation between the short-circuit current and open circuit voltage for the proposed structures under optimal conditions. At 0 V, all architectures exhibit the maximum current, which rapidly declines at 1.3 V, except when $PC_{60}BM$ is used as the electron transport layer. For the FTO/$PC_{60}BM$/$CsSnBr_3$/MoO_3/Au structure, the current approaches zero at 1.18 V, although it demonstrates the highest current density of 17.39 mA cm^{-2} among all configurations.

Quantum efficiency (QE) is the effectiveness with which incoming photons are transformed into charge carriers, thereby contributing to the photocurrent. Fig. 10(b) demonstrates the variation in the quantum efficiency as it correlates with changes in the light wavelength. The wavelength of light was varied from 300 nm to 800 nm to assess the effectiveness of

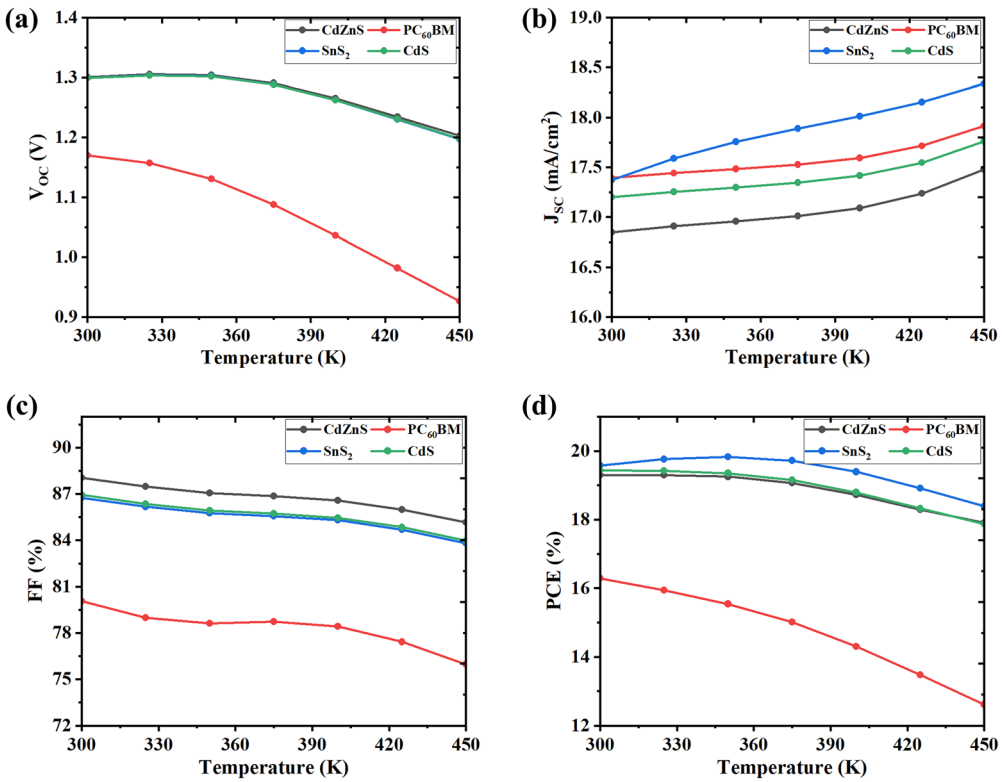

Fig. 9 Effect of the temperature on the performance parameters, (a) V_{OC}, (b) J_{SC}, (c) FF, and (d) PCE, of the suggested structures.

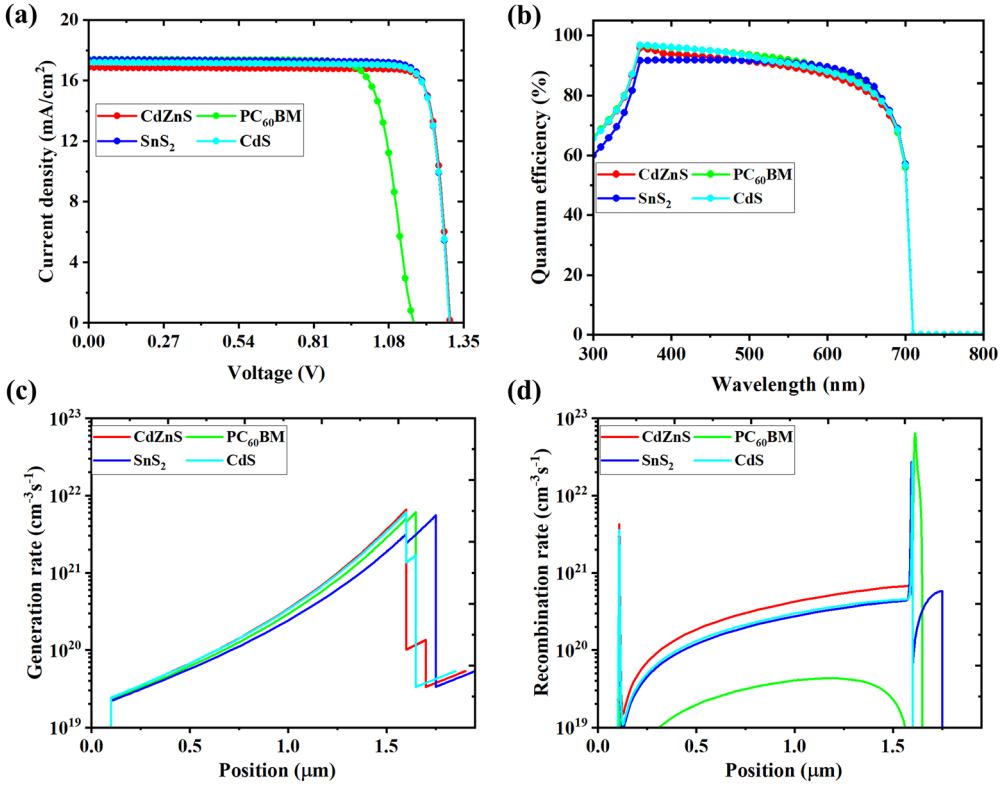

Fig. 10 (a) Current density *versus* voltage characteristics curve, (b) quantum efficiency curves, (c) generation rates, and (d) recombination rates of the optimized structures.

the structures in absorbing light. At a wavelength of 300 nm, the quantum efficiency is approximately 60% for the structures, but it shows a considerable improvement at longer wavelengths. At a wavelength of 350 nm, all proposed structures demonstrate almost 100% quantum efficiency and sustain over 80% efficiency up to 700 nm. Beyond 700 nm, the quantum efficiency sharply diminishes and ultimately approaches zero.

3.9. Generation and recombination rates

Charge carrier generation transpires when a photon with energy beyond the bandgap of the absorber material strikes it. It necessitates the carriers' shift from the valence band to the conduction band. Conversely, recombination in solar cells occurs *via* the production of electron–hole pairs, hence diminishing the overall quantity of charge carriers. Fig. 10(c) illustrates the generation rates of the optimal PSCs in relation to the substance thickness. In the FTO/CdZnS/$CsSnBr_3$/MoO_3/Au configuration, the peak generation rate of 10^{22} cm^{-3} s^{-1} occurs at 1.6 μm, which is also seen in the rest of the devices, suggesting that all devices exhibit enhanced light absorption at higher depths within the substance. The variation in the peak generation depth arises from changes in the optical absorption properties, layer thicknesses, and chemical makeup of the absorber layers in each device.[70]

Fig. 10(d) depicts the recombination rates of the final optimized structures with the material thickness. Two major peaks in the recombination rates are seen at depths of 0.15 μm and 1.6 μm. Most of the time, the structures show relatively lower and unchanged recombination rates of less than 10^{22} cm^{-3} s^{-1}. The recombination rate decreases at higher depths, either because there are fewer defects or because the material inside the larger part of the absorber is more uniform. This trend shows how important it is to pay attention to the quality of materials and interfacial engineering in order to reduce recombination losses, especially at surfaces and interfaces.[71]

3.10. Comparison with previous studies

Researchers are widely investigating perovskite solar structures to establish a solid foundation for the modern industry.[68,72] Further improvements could lead to ground-breaking technology that may play a crucial role in mitigating the energy crisis in the next century. A significant number of studies have already been conducted by researchers around the world. In this regard, $CsSnBr_3$-based PSCs can play an important role. The PCE of $CsSnBr_3$-based PSCs has reached a good level, as reported in the literature. To understand the efficiency of our simulated structures, a brief comparison with relevant previous studies is presented in Table 3. The particular absorber material, *i.e.*, $CsSnBr_3$ perovskite, is comparatively excellent for both experimental and theoretical studies due to its competitive durability. A study by L. Cau *et al.*[73] revealed that a facile, low-cost, room-temperature method, namely, coprecipitation using ethanol and salicylic acid, stabilizes $CsSnBr_3$ perovskites by preventing Sn^{2+} oxidation through surface coordination, which leads to exceptional oxygen and moisture resistance for over 10 days. Studies on $CsSnBr_3$-based PSC structures have

Table 3 Comparison of relevant previous studies with this study

Type	Structure	V_{OC} (V)	J_{SC} (mA cm^{-2})	FF (%)	PCE (%)	Year	Ref.
T	FTO/CdZnS/$CsSnBr_3$/MoO_3/Au	1.30	16.85	88.04	19.29	2025	This work
T	FTO/$PC_{60}BM$/$CsSnBr_3$/MoO_3/Au	1.17	17.39	80.06	16.29	2025	This work
T	FTO/SnS_2/$CsSnBr_3$/MoO_3/Au	1.30	17.37	86.74	19.58	2025	This work
T	FTO/CdS/$CsSnBr_3$/MoO_3/Au	1.30	17.20	86.93	19.43	2025	This work
T	FTO/ZnO/$CsSnBr_3$/WSe_2/Se	1.39	25.81	88.18	31.62	2025	53
T	ITO/WS_2/$CsSnBr_3$/V_2O_5/Ni	1.42	19.39	89.87	24.69	2025	75
T	Al/FTO/SnS_2/$CuSbS_2$/Ni	1.39	25.09	88.54	31.09	2025	76
T	FTO/TiO_2/$CsSnBr_3$/P3HT/Au	1.31	18.01	75.80	17.94	2023	77
T	ITO/WS_2/$CsSnBr_3$/Cu_2O/Au	1.42	19.39	89.87	24.69	2025	78
T	ITO/PCBM/$CsSnBr_3$/Cu_2O/Au	1.23	19.16	83.72	19.73	2024	79
T	ITO/PCBM/$CsSnBr_3$/Cu_2BaSnS_4/Au	1.33	17.43	83.21	19.25	2025	80
T	ITO/IGZO/$CsSnBr_3$/Cu_2O/Au	1.33	19.17	85.65	21.88	2024	81
T	FTO/SnO_2/$CsSnBr_3$/CuI/Au	1.19	16.94	84.19	17.06	2023	52
P	FTO/TiO_2/$CsSnBr_3$/MoO_3/Al	0.38	11.96	34.00	1.50	2021	82
P	FTO/TiO_2/$CsSnBr_3$:SnF_2/Spiro-OMeTAD/Au	0.40	9.10	56.00	2.04	2016	83
P	ITO/TiO_2/$CsSnBr_3$/Spiro-OMeTAD/Au	0.85	21.23	58.00	10.46	2016	84

*T = Theoretical and P = Practical.

progressed over the past decade, encompassing both fabrication techniques and performance optimization. In the case of deposition of this material, the epitaxial growth of lead-free $CsSnBr_3$ films on silicon *via* pulsed laser deposition creates a high-mobility P-type with a type-II heterojunction, efficiently enabling a self-powered photodetector with a high switch ratio ($>10^4$) and millisecond-level response times, which is stated by A. Wang *et al.* from ref. 74. In summary, these studies are the potential proof to test and reveal the potential of $CsSnBr_3$ perovskites for future applications.

4. Machine learning-based calculations

4.1. Correlation matrix analysis

Fig. 11 presents the correlation matrix with the linear relationships between the device's material parameters and PV performance output obtained from the SCAPS-1D-generated dataset. A dominant positive correlation is observed between the absorber acceptor density (absorber N_A) and open-circuit voltage, V_{OC} ($r \approx 0.79$). It is an indicator that enhanced p-type doping strengthens the internal electric field and raises the quasi-Fermi level splitting.[85,86] However, the same parameter exhibits a strong negative correlation with the short-circuit current density, J_{SC} ($r \approx -0.91$), which signifies that excessive doping increases trap-assisted recombination, reducing the number of photogenerated carriers reaching the electrodes.

The robust positive relationship between the V_{OC} and FF ($r \approx 0.86$) indicates that an increase in the voltage directly aids in charge collection and lower resistive losses. This trend corresponds with the properties of Sn-based perovskites and is consistent with previous studies indicating that V_{OC} is heavily affected by recombination behaviour.[87] The absorber thickness exhibits an association with the PCE ($r \approx 0.29$) because a thicker $CsSnBr_3$ layer increases photon absorption without negatively affecting the voltage FF. HTL N_A also demonstrates a positive correlation with the efficiency ($r \approx 0.30$). This finding indicates that adequate hole transport improvement moderately enhances the PCE. In contrast, the ETL donor density (ETL N_D) shows a weak negative correlation ($r \approx -0.39$) with device efficiency. This may imply that excessive n-type doping in the ETL may distort the band alignment and elevate recombination at the ETL/$CsSnBr_3$ interface. Together, the heatmap in Fig. 11 reveals the parameters absorber N_A, HTL N_A, absorber thickness, and ETL N_D as the most critical parameters for boosting the $CsSnBr_3$ PSC's electrical performance.

4.2. Machine learning model accuracy evaluation

Fig. 12 compares the predictive accuracy of four regression models, namely, linear regression (LR), multilayer perceptron (MLP) regression, random forest (RF), and XGBoost (XGB), against SCAPS-simulated photovoltaic parameters. The plots in Fig. 12 clearly show how differently each regression model behaves when trying to predict the photovoltaic parameters of the simulated PSCs. Each row represents one algorithm, and the contrast between them highlights how well or how poorly

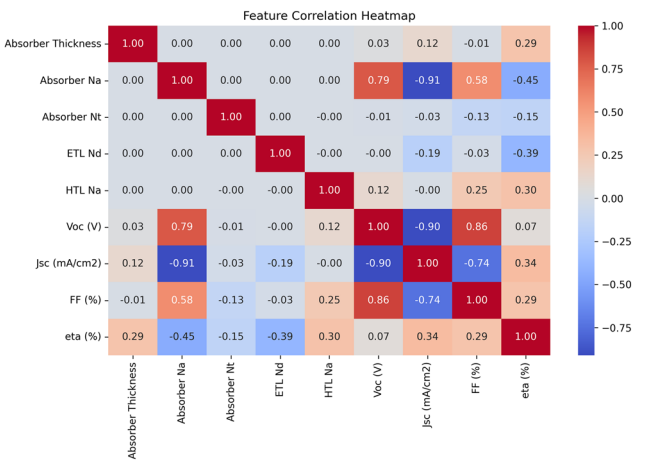

Fig. 11 Feature correlation heatmap for the machine learning dataset, highlighting the degree of dependency between device design parameters and output metrics.

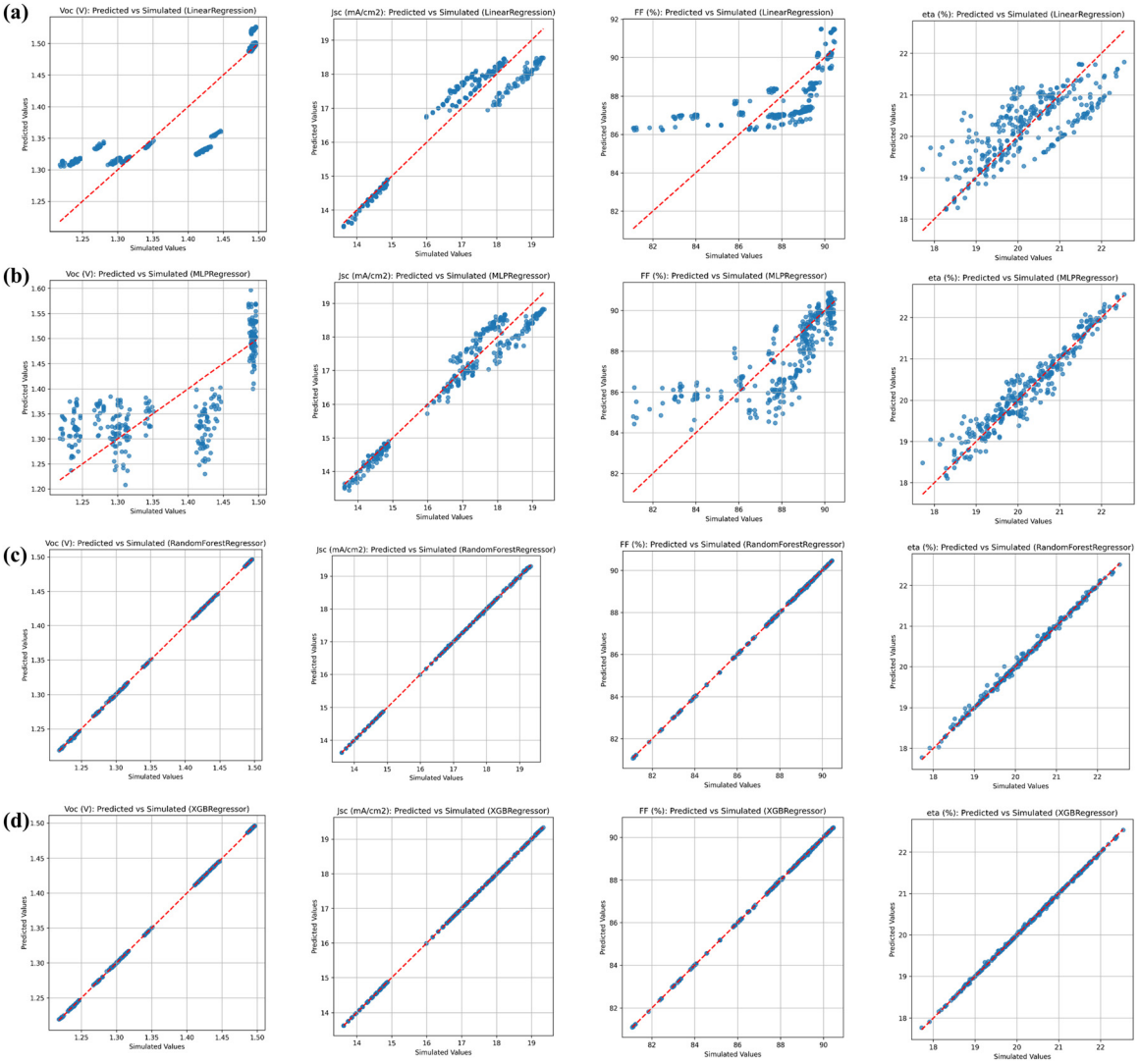

Fig. 12 Predictive accuracy plots for the performance parameters of ML models: (a) linear regression, (b) MLP regression, (c) random forest, and (d) extreme gradient boost models.

they can follow the nonlinear physics that govern device performance. The scatter points in the LR and MLP regression plots display noticeable dispersion around the ideal reference line, particularly for V_{OC} and FF. This indicates their insufficient ability to capture nonlinear relationships among parameters such as absorber doping, defect density, and ETL/HTL charge transport characteristics. In real devices, changes in the absorber doping, defect density, recombination rates, and interface quality all interact with one another in nonlinear ways. Because linear regression cannot follow these combined effects, its predictions fall widely above and below the ideal 1 : 1 line, making it the weakest performer. The neural network model performs slightly better than linear regression, but its predictions are still noticeably scattered, especially for the V_{OC} and FF. Importantly, MLPs are designed to learn nonlinear patterns; their accuracy depends heavily on the depth of the network, the number of neurons, and the training pattern. If the network is too simple or does not fully learn subtle patterns-such as slight variations in the mobility or trap density-it will miss important physical behaviors. This is observed in the uneven prediction clusters that do not align perfectly with the reference line.

The random forest model shows a significantly improved alignment, with most points for V_{OC}, J_{SC}, FF, and η (eta) clusters closely following the reference line. This improvement arises from its capability to model nonlinear and multidimensional parameter interactions using ensemble decision trees. A significant improvement appears in the next set of plots. The RF model predicts values that lie very close to the simulated results because RF uses many individual decision trees, and these trees individually capture different parts of the nonlinear relationships. When combined, the trees collectively learn the complex interactions between parameters such as absorber thickness, ETL/HTL properties, and recombination paths. The tight clustering around the reference line shows that the model handles multidimensional, nonlinear behaviour much more effectively.

Among all models, the XGB regressor exhibits the highest predictive fidelity. This model works by building trees one at a time, where each new tree corrects the errors remaining from the previous ones. The scatter points for all four performance metrics lie almost perfectly on the reference line. This phenomenon demonstrates minimal error and exceptional generalization capability. The superiority of XGBoost arises from its gradient-boosted decision tree architecture, which sequentially refines weak learners and minimizes both bias and variance. XGBoost consistently emerges as the most accurate model for nonlinear PV modeling. Fig. 12 finally confirms that XGBoost is the most reliable algorithm for accurately predicting $CsSnBr_3$ solar cell performance to capture even subtle dependencies between electrical parameters and PV output for our study.

4.3. SHAP interpretability analysis

While SHAP analysis identifies the absorber doping concentration as the most influential parameter, it is important to assess whether this reflects true physical behaviour or arises from dataset bias.[59] In this study, the dominance of the absorber doping is not solely a data-driven outcome but is strongly supported by device physics. The absorber doping concentration directly affects the built-in electric field, carrier separation efficiency, and recombination rate, thereby significantly influencing key photovoltaic parameters such as V_{OC}, FF, and PCE. Fig. 13 provides a comprehensive SHAP-based interpretation of how different physical parameters influence the predicted photovoltaic outputs (V_{OC}, J_{SC}, FF, and PCE), with the absorber acceptor density (N_A) emerging as the most dominant contributor across all metrics. For V_{OC}, higher absorber N_A consistently produces positive SHAP values, showing that stronger p-type doping enhances the internal electric field and improves charge separation, while HTL N_A acts as the second-most important factor by facilitating hole extraction and lowering interfacial recombination. In the case of J_{SC}, the SHAP trends reverse; absorbed N_A shifts toward negative contributions, indicating that excessive p-type doping intensifies bulk recombination and reduces photocurrent, whereas the absorber thickness and

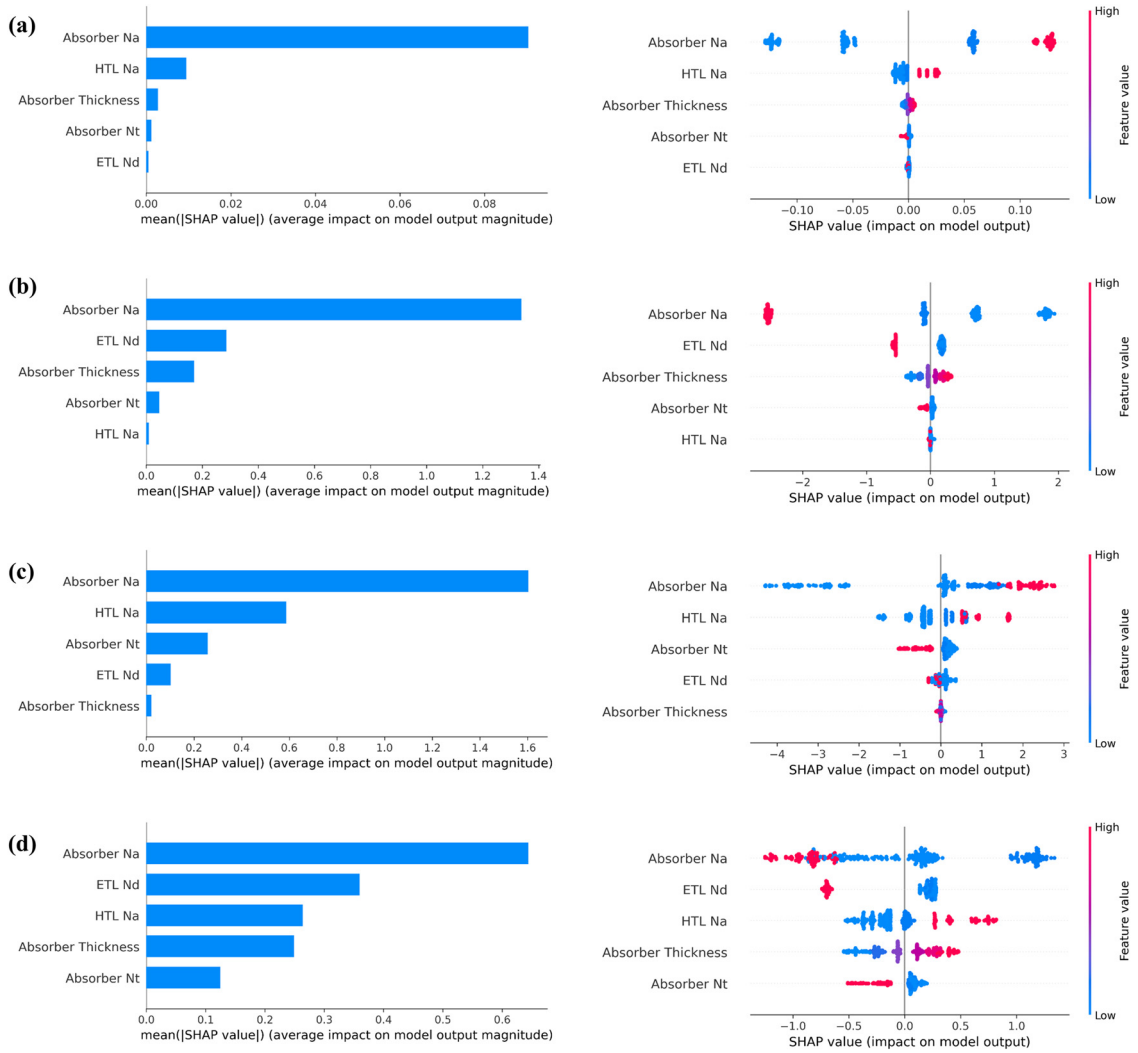

Fig. 13 Effect of variations in the electrical properties on the performance parameters, (a) V_{OC} (V), (b) J_{SC} (mA cm^{-2}), (c) FF (%), and (d) PCE (%), determined using SHAP plots.

ETL donor density (N_D) contribute positively by improving light absorption and electron extraction. For the FF, the absorber N_A again plays the leading role, as moderate doping smooths charge transport pathways and minimizes resistive losses, while HTL N_A further strengthens hole mobility and interface quality. The PCE analysis shows a similar pattern, as the absorber N_A remains the strongest determinant, followed by ETL N_D and HTL N_A, reflecting the combined importance of balanced carrier extraction in both transport layers. However, the SHAP distributions reveal that overly high doping levels eventually push contributions into the negative domain due to increased recombination. The absorber thickness has a positive but moderate influence, consistent with the enhancement of optical absorption up to an optimal level. Overall, the SHAP results clearly demonstrate that device performance may be tuned by balancing the absorber doping, transport layer carrier densities, and absorber optical depth. The above-mentioned parameters offer strong physical interpretability and nearly align with behaviours predicted by SCAPS simulations.

5. Conclusions

This study investigates and optimizes $CsSnBr_3$-based perovskite solar cells to evaluate their efficiency as an absorber material. Four unique ETL materials are employed to construct the structures, considering the alignment of energy bands. Upon examining the influence of the acceptor and defect densities of the absorber, the thicknesses of the electron transport layer (ETL) and hole transport layer (HTL), the donor and defect densities in the ETL, and the acceptor and defect densities in the HTL, it is evident that these factors exert a minimal impact on the efficiency of the devices. Taking into account the efficiency and manufacturing capabilities, an optimized thickness of 1500 nm is selected for the absorber in all structures. The improved devices exhibit enhanced efficiency when the series resistance is minimal and the shunt resistance is maximal. The structures exhibit optimal efficiency at ambient temperature. The optimized structures exhibit an elevated carrier production rate and a decreased carrier recombination rate. Although this study is based on numerical simulations, efforts have been made to validate the obtained results through benchmarking with previously reported experimental and theoretical studies. Machine learning analysis further validates the simulation outcomes by identifying absorber N_A as the most critical factor influencing all PV metrics, followed by the ETL N_D, HTL N_A, and absorber thickness. The strong agreement between SCAPS results and ML-derived feature importance demonstrates that the hybrid SCAPS-ML approach is a powerful tool for guiding the future optimization and design of $CsSnBr_3$ and other lead-free PSCs. Post optimization, the configuration of FTO/SnS_2/$CsSnBr_3$/MoO_3/Au exhibits the maximum efficiency of 19.58% compared to other structures.

Author contributions

M. Humayet Islam: writing – original draft, data curation, formal analysis, methodology, investigation, visualization, software, conceptualization, and writing – review and editing. **Tanzir Ahamed:** writing – review and editing, validation, visualization, software, resources, investigation, supervision, methodology, formal analysis, and data curation. **M. Shihab Uddin:** writing – review and editing, visualization, validation, supervision, software, resources, project administration, methodology, investigation, funding acquisition, formal analysis, data curation, conceptualization, and writing–original draft. **M. Jalal Uddin:** writing – review and editing, validation, and visualization. **M. M. Alam:** supervision, methodology, software, resources, project administration, investigation, funding acquisition, formal analysis, conceptualization, and writing – review and editing. **Md. Ali Hossain:** writing–review and editing and visualization. **Md Masum Billah:** writing – review and editing, visualization, and resources. **Md. Hasanuzzaman Dipu:** writing – review and editing and visualization. **Fernaz Narin Nur:** writing – review and editing and methodology.

Conflicts of interest

The authors declare that they have no known competing financial interests or personal relationships that could have appeared to influence the work reported in this paper.

Data availability

The datasets used and/or analyzed during the current study are available from the corresponding author upon reasonable request.

Acknowledgements

This research did not receive any specific grant from funding agencies in the public, commercial, or not-for-profit sectors. The authors provide humble thanks to Prof. M. Burgelman for the software simulation package of SCAPS-1D without any financial transaction.

References

1 D. J. Arent, A. Wise and R. Gelman, The status and prospects of renewable energy for combating global warming, *Energy Econ.*, 2011, **33**, 584–593.
2 T. Abbasi and S. A. Abbasi, Is the use of renewable energy sources an answer to the problems of global warming and pollution?, *Crit. Rev. Environ. Sci. Technol.*, 2012, **42**, 99–154.
3 P. Fornasiero and M. Graziani, *Renewable resources and renewable energy: a global challenge*, CRC press, 2011.
4 F. Rayhan, M. H. Rahman, S. Rana, D. Das Ria, J. I. Chy, M. S. Hosen, T. Ahamed, J. Sarpong, K. Yegbe and M. S. Uddin, Unveiling the potential of non-toxic Ge based perovskite material for all inorganic solar cells using multiple ETLs, *Photonics Nanostructures - Fundam. Appl.*, 2025, **66**, 101425, DOI: 10.1016/j.photonics.2025.101425.

5 J. Y. Kim, J.-W. Lee, H. S. Jung, H. Shin and N.-G. Park, High-efficiency perovskite solar cells, *Chem. Rev.*, 2020, **120**, 7867–7918.
6 R. Sharma, A. Sharma, S. Agarwal and M. S. Dhaka, Stability and efficiency issues, solutions and advancements in perovskite solar cells: A review, *Sol. Energy*, 2022, **244**, 516–535.
7 M. Jeong, I. W. Choi, E. M. Go, Y. Cho, M. Kim, B. Lee, S. Jeong, Y. Jo, H. W. Choi and J. Lee, Stable perovskite solar cells with efficiency exceeding 24.8% and 0.3-V voltage loss, *Science*, 2020, **369**, 1615–1620.
8 K. Dey, B. Roose and S. D. Stranks, Optoelectronic properties of low-bandgap halide perovskites for solar cell applications, *Adv. Mater.*, 2021, **33**, 2102300.
9 T. Ahamed, I. Rahaman, S. Karmakar, M. A. Halim and P. K. Sarkar, Thickness optimization and the effect of different hole transport materials on methylammonium tin iodide (CH3NH3SnI3)-based perovskite solar cell, *Emergent Mater.*, 2023, **6**, 175–183, DOI: 10.1007/s42247-022-00405-8.
10 F. Giustino and H. J. Snaith, Toward lead-free perovskite solar cells, *ACS Energy Lett.*, 2016, **1**, 1233–1240.
11 G. Schileo and G. Grancini, Lead or no lead? Availability, toxicity, sustainability and environmental impact of lead-free perovskite solar cells, *J. Mater. Chem. C*, 2021, **9**, 67–76.
12 G. F. I. Toki, M. K. Hossain, M. Shihab Uddin, A. M. Tawfeek, S. Rabhi, M. A. Darwish, R. Haldhar, D. K. Dwivedi, J. Madan and R. Pandey, Unveiling the potential of lead-free Cs2AgBi0.75Sb0.25Br6 double perovskite solar cells with multilayer charge transport for 30% efficiency, *Inorg. Chem. Commun.*, 2024, **165**, 112439, DOI: 10.1016/j.inoche.2024.112439.
13 S. Mushtaq, S. Tahir, A. Ashfaq, R. S. Bonilla, M. Haneef, R. Saeed, W. Ahmad and N. Amin, Performance optimization of lead-free MASnBr3 based perovskite solar cells by SCAPS-1D device simulation, *Sol. Energy*, 2023, **249**, 401–413.
14 R. Kour, S. Arya, S. Verma, J. Gupta, P. Bandhoria, V. Bharti, R. Datt and V. Gupta, Potential substitutes for replacement of lead in perovskite solar cells: a review, *Glob. Chall.*, 2019, **3**, 1900050.
15 Q. Zhang, F. Hao, J. Li, Y. Zhou, Y. Wei and H. Lin, Perovskite solar cells: must lead be replaced–and can it be done?, *Sci. Technol. Adv. Mater.*, 2018, **19**, 425–442.
16 L. Serrano-Lujan, N. Espinosa, T. T. Larsen-Olsen, J. Abad, A. Urbina and F. C. Krebs, Tin- and lead-based perovskite solar cells under scrutiny: An environmental perspective, *Adv. Energy Mater.*, 2015, **5**, 1–5, DOI: 10.1002/aenm.201501119.
17 W. Ke, C. C. Stoumpos and M. G. Kanatzidis, ''Unleaded'' perovskites: status quo and future prospects of tin-based perovskite solar cells, *Adv. Mater.*, 2019, **31**, 1803230.
18 M. M. Saad and S. E. A. Yousif, Structural and optoelectronic properties of CsSnBr3 metal halide perovskite as promising materials toward novel-generation optoelectronics, *Chalcogenide Lett.*, 2022, **19**, 153–162, DOI: 10.15251/CL.2022.192.153.
19 M. I. Kholil, M. T. H. Bhuiyan, M. A. Rahman, M. S. Ali and M. Aftabuzzaman, Influence of molybdenum and technetium doping on visible light absorption, optical and electronic properties of lead-free perovskite CsSnBr 3 for optoelectronic applications, *RSC Adv.*, 2021, **11**, 2405–2414.
20 A. El Badraoui, S. Dahbi, N. Tahiri, O. El Bounagui and H. Ez-Zahraouy, A DFT study of the electronic structure, optical and thermoelectric properties of perovskite CsSnBr3 compound under strains effect: photovoltaic applications, *Mod. Phys. Lett. B*, 2024, **38**, 2350237.
21 A. Kumar, N. Pandey, D. Punetha and S. Chakrabarti, Investigation of structural and optical properties of rGo alloyed CsSnBr3 for solar cell application, *Physics, Simulation, and Photonic Engineering of Photovoltaic Devices XII*, SPIE, 2023, pp. 69–76.
22 P. E. Marchezi, F. L. De Araújo, R. Szostack, J. C. Germino, E. M. Therézio, A. Marletta and A. F. Nogueira, Reduced graphene oxide in perovskite solar cells: the influence on film formation, photophysics, performance, and stability, *J. Mater. Chem. C*, 2021, **9**, 14648–14658, DOI: 10.1039/D1TC01360B.
23 L. Cao, S.-M. Gu, B. Liu, L. Huang, J. Zhang, Y. Zhu and J. Wang, Highly Ambient Stable CsSnBr3 Perovskite via a New Facile Room-Temperature ''Coprecipitation'' Strategy, *ACS Appl. Mater. Interfaces*, 2023, **15**, 30409–30416.
24 S. A. Dar and B. S. Sengar, Analysis of lead free CsSnBr3 based perovskite solar cells utilizing numerical modeling, *Phys. Scr.*, 2024, **99**, 65013.
25 B. V. Kheswa, Numerical optimization of all-inorganic CsSnBr3 perovskite solar cells: the observation of 27% power conversion efficiency, *Phys. Scr.*, 2024, **100**, 15933.
26 R. Ferdous, G. Hashmi and F. Montashir, Design and Simulation of High-Efficiency CH 3 NH 3 PbI 3/CsSnBr 3-based Bilayer Perovskite Solar Cell, in: 2024 7th International Conference on Development in Renewable Energy Technology (ICDRET), IEEE, 2024: pp. 1–6.
27 D. Fang, Y. Tong, F. Xu, B. Mi, D. Cao and Z. Gao, Preparation of CsSnBr3 perovskite film and its all-inorganic solar cells with planar heterojunction, *J. Solid State Chem.*, 2021, **294**, 121902.
28 D. Moghe, L. Wang, C. J. Traverse, A. Redoute, M. Sponseller, P. R. Brown, V. Bulović and R. R. Lunt, All vapor-deposited lead-free doped CsSnBr3 planar solar cells, *Nano Energy*, 2016, **28**, 469–474.
29 L.-J. Chen, C.-R. Lee, Y.-J. Chuang, Z.-H. Wu and C. Chen, Synthesis and Optical Properties of Lead-Free Cesium Tin Halide Perovskite Quantum Rods with High-Performance Solar Cell Application, *J. Phys. Chem. Lett.*, 2016, **7**, 5028–5035, DOI: 10.1021/acs.jpclett.6b02344.
30 Y. Chu, Y. Hu and Z. Xiao, First-Principles Insights into the Stability Difference between ABX_3 Halide Perovskites and Their A_2 BX_6 Variants, *J. Phys. Chem. C*, 2021, **125**, 9688–9694, DOI: 10.1021/acs.jpcc.1c02312.
31 I. Paul, B. C. Biswas, A. I. Shimul, S. AlFaify, A. M. Elbasiony, M. Benghanem and Md. A. Rahman, Performance analysis of halide perovskites Be3NX3 (X = F, Cl, Br) with multiple

hole and electron transport layers using DFT, SCAPS-1D and deep learning methods, *J. Phys. Chem. Solids*, 2026, **211**, 113493, DOI: 10.1016/j.jpcs.2025.113493.

32 M. S. Reza, A. Ghosh, A. I. Shimul, S. H. Nabil, M. Akter, A. R. Chaudhry, D. R. Sobuj, Y. Anil Kumar, S. Biswas, K. Alam and M. Maqsood, Simulation and machine learning driven optimization of Rb_2 $SnBr_6$ -based lead-free perovskite solar cells using diverse ETLs for enhanced photovoltaic performance, *Mater. Adv.*, 2025, **6**, 9602–9626, DOI: 10.1039/D5MA00955C.

33 A. S. Sarker, A. I. Shimul, M. Tarekuzzaman and B. C. Biswas, Eco-friendly Cs2SnGeCl6 perovskite absorber: A combined numerical simulation and machine learning analysis for high efficiency solar cells, *Mater. Today Electron.*, 2026, **16**, 100208, DOI: 10.1016/j.mtelec.2026.100208.

34 M. S. Uddin, M. K. Hossain, M. B. Uddin, G. F. I. Toki, M. Ouladsmane, M. H. K. Rubel, D. I. Tishkevich, P. Sasikumar, R. Haldhar and R. Pandey, An In-Depth Investigation of the Combined Optoelectronic and Photovoltaic Properties of Lead-Free Cs_2 $AgBiBr_6$ Double Perovskite Solar Cells Using DFT and SCAPS-1D Frameworks, *Adv. Elect. Mater.*, 2024, **10**, 2300751, DOI: 10.1002/aelm.202300751.

35 J. Seo, J. H. Noh and S. Il Seok, Rational strategies for efficient perovskite solar cells, *Acc. Chem. Res.*, 2016, **49**, 562–572.

36 L. Qiu, D. Mei, W.-H. Chen, Y. Yuan, L. Song, L. Chen, B. Bai, P. Du and J. Xiong, Organic-inorganic hybrid electron transport layer of PVP-doped SnO2 for high-efficiency stable perovskite solar cells, *Solar Energy Mater. Solar Cells*, 2022, **248**, 112032.

37 I. Alam, R. Mollick and M. A. Ashraf, Numerical simulation of Cs2AgBiBr6-based perovskite solar cell with ZnO nanorod and P3HT as the charge transport layers, *Phys. B*, 2021, **618**, 413187, DOI: 10.1016/j.physb.2021.413187.

38 Q. Fatima, A. A. Haidry, H. Zhang, A. El Jery and M. Aldrdery, A critical review on advancement and challenges in using TiO2 as electron transport layer for perovskite solar cell, *Mater. Today Sustainability*, 2024, 100857.

39 Y. Shen, K. Deng and L. Li, Spiro-OMeTAD-Based Hole Transport Layer Engineering toward Stable Perovskite Solar Cells, *Small Methods*, 2022, **6**, 2200757.

40 C. Luo, P. Jiang, L. Hu, M. Bian, L. Wan, H. Niu, X. Mao, R. Zhou and J. Xu, Constructing CdS-based electron transporting layers with efficient electron extraction for perovskite solar cells, *IEEE J. Photovolt.*, 2021, **11**, 1014–1021.

41 A. A. Khan, M. Noman and S. T. Jan, Investigating the compatibility of kesterite and zinc charge transport layers with inorganic germanium perovskite solar cells, *Opt. Quantum Electron.*, 2025, **57**, 1–35.

42 M. S. Reza, M. F. Rahman, M. S. Reza, M. R. Islam, U. U. Rehman, A. R. Chaudhry and A. Irfan, Rubidium based new lead free high performance perovskite solar cells with SnS2 as an electron transport layer, *Mater. Today Commun.*, 2024, **39**, 108714.

43 J. Xie, V. Arivazhagan, K. Xiao, K. Yan, Z. Yang, Y. Qiang, P. Hang, G. Li, C. Cui and X. Yu, A ternary organic electron transport layer for efficient and photostable perovskite solar cells under full spectrum illumination, *J. Mater. Chem. A*, 2018, **6**, 5566–5573.

44 J. Wang, X. Zou, J. Zhu, J. Cheng, D. Chen, X. Bai, Y. Yao, C. Chang, X. Yu, B. Liu, Z. Zhou and G. Li, Effect of Optimization of TiO2 Electron Transport Layer on Performance of Perovskite Solar Cells with Rough FTO Substrates, *Materials*, 2020, **13**, 2272, DOI: 10.3390/ma13102272.

45 S. Bonomi, M. Patrini, G. Bongiovanni and L. Malavasi, Versatile vapor phase deposition approach to cesium tin bromide materials $CsSnBr_3$, $CsSn_2$ Br_5 and Cs_2 $SnBr_6$, *RSC Adv.*, 2020, **10**, 28478–28482, DOI: 10.1039/D0RA04680A.

46 R. Ukai, Y. Wasai, Y. Izumi and H. Shirai, Solution-Processed Monolithic Tandem Perovskite/n-Si Hybrid Solar Cells Using MoO3/InZnO Bilayer-Based Interconnecting and Window Layers, *Crystals*, 2024, **14**, 68, DOI: 10.3390/cryst14010068.

47 F. U. Kosasih, E. Erdenebileg, N. Mathews, S. G. Mhaisalkar and A. Bruno, Thermal evaporation and hybrid deposition of perovskite solar cells and mini-modules, *Joule*, 2022, **6**, 2692–2734, DOI: 10.1016/j.joule.2022.11.004.

48 A. Kumar and S. Singh, Computational simulation of metal doped lead-free double perovskite (Cs2AgBi0.75Sb0.25Br6) solar cell using solar cell capacitance simulator, *Mater. Today: Proc.*, 2021, **44**, 2215–2222, DOI: 10.1016/j.matpr.2020.12.356.

49 M. S. Uddin, S. Rana, M. K. Hossain, A. Kumar, P. Kanjariya, P. S. Bains, R. Sharma, H. Kumar, G. Tank, A. A. Awadh Bahajjaj and V. K. Mishra, Performance improvement and optimization of $Cs_2TiI_2Br_4$ perovskite solar cells with diverse charge transport materials via numerical analysis, *J. Phys. Chem. Solids*, 2025, **198**, 112486, DOI: 10.1016/j.jpcs.2024.112486.

50 M. K. Hossain, K. M. Sadat, M. S. Uddin, A. K. Datta, P. Kanjariya, M. S. Reddy, R. Kalia, B. Selvaraj, A. A. A. Bahajjaj, R. Balachandran, A. Hajjiah and R. Haldhar, An investigation of hole transport layers and electron transport layers to produce highly efficient K2TiI6-based perovskite solar cells, *Sci. Rep.*, 2025, **15**, 19014, DOI: 10.1038/s41598-025-98351-y.

51 T. Ahamed, F. Rayhan, I. Rahaman, Md. H. Rahman, Md. M. Hasan Bappy, T. Ahammed and S. Ghosh, Optimization of Buffer Layers for CZTSSe Solar Cells through Advanced Numerical Modelling, *J. Phys. Chem. Solids*, 2025, 112744, DOI: 10.1016/j.jpcs.2025.112744.

52 S. Khatoon, S. Kumar Yadav, V. Chakraborty, J. Singh and R. Bahadur Singh, A simulation study of all inorganic lead-free CsSnBr3 tin halide perovskite solar cell, *Mater. Today: Proc.*, 2023, S2214785323020631, DOI: 10.1016/j.matpr.2023.04.167.

53 B. V. Kheswa and S. Majola, Simulation of novel $CsSnBr_3$ perovskite solar cells achieving efficiency of 31.62%, *Phys. Scr.*, 2025, **100**, 015017, DOI: 10.1088/1402-4896/ad986e.

54 J. Jia, R. Wang and H. Mu, Exciton dynamics and photoresponse behavior of the *in situ* annealed $CsSnBr_3$ perovskite films synthesized by thermal evaporation,

Nanotechnology, 2022, **33**, 345503, DOI: 10.1088/1361-6528/ac6f11.

55 M. S. Shamna and K. S. Sudheer, Device modeling of Cs2PtI6-based perovskite solar cell with diverse transport materials and contact metal electrodes: a comprehensive simulation study using solar cell capacitance simulator, *J. Photon. Energy*, 2022, **12**(3), 032211, DOI: 10.1117/1.JPE.12.032211.

56 M. A. Benatallah, A. Elmohri, Y. I. Bouderbala, M. W. Alam and S. Rabhi, Boosting Efficiency in Flexible Perovskite Solar Cells with Novel HTLs and ETLs: A drift-diffusion numerical study of CBz-PAI Interlayers and MXene Back Contacts, *Adv. Theory Sims.*, 2025, **8**, 2401161, DOI: 10.1002/adts.202401161.

57 S. Rabhi, G. M. Alsulaim, Y. I. Bouderbala and M. W. Alam, Enhancing inverted perovskite solar cells: The role of o-OMe-PEAI interlayer in performance with MXene as alternative front contacts, *Inorg. Chem. Commun.*, 2025, **175**, 114096, DOI: 10.1016/j.inoche.2025.114096.

58 M. K. Hossain, G. F. I. Toki, A. Kuddus, M. H. K. Rubel, M. M. Hossain, H. Bencherif, Md. F. Rahman, Md. R. Islam and M. Mushtaq, An extensive study on multiple ETL and HTL layers to design and simulation of high-performance lead-free CsSnCl3-based perovskite solar cells, *Sci. Rep.*, 2023, **13**, 2521, DOI: 10.1038/s41598-023-28506-2.

59 T. Ahamed, Md. M. H. Bappy, M. R. Islam, Md. S. Uddin, Md. A. Hossain and T. Ahammed, Performance optimization and machine learning-guided parameter sensitivity analysis of lead-free $KGeCl_3$ perovskite solar cells, *RSC Adv.*, 2026, **16**, 8985–9011, DOI: 10.1039/D6RA00262E.

60 L. Haryński, A. Olejnik, K. Grochowska and K. Siuzdak, A facile method for Tauc exponent and corresponding electronic transitions determination in semiconductors directly from UV–Vis spectroscopy data, *Opt. Mater.*, 2022, **127**, 112205, DOI: 10.1016/j.optmat.2022.112205.

61 B. Bibi, W. Ur Rahman, N. Us Sama, L. Guan, S. Hatim Shah and Z. Liu, Machine Learning-Driven Optimization of Transport Layer Parameters in CsSn0.5 Ge0.5 I3 Perovskite Solar Cells, *IEEE Access*, 2025, **13**, 185416–185432, DOI: 10.1109/ACCESS.2025.3626236.

62 N. A. Tukadiya, Z. D. Ponkiya, N. Joshi, D. Upadhyay and P. K. Jha, Machine learning and SCAPS-1D based prediction and validation of RbGeBr 3 perovskite solar cell, *Sol. Energy*, 2025, **300**, 113760, DOI: 10.1016/j.solener.2025.113760.

63 N. Bouri, T. A. Geleta, K. W. Guji, A. Hammad, S. Rabhi and K. Nouneh, Resistance dynamics in a solar cell with novel lead-free perovskite absorbers (LiMgI3 and NaMgI3): Performance optimization using SCAPS-1D simulation and impedance spectroscopy, *J. Phys. Chem. Solids*, 2025, **207**, 112972, DOI: 10.1016/j.jpcs.2025.112972.

64 T. Ahamed, M. S. Uddin, T. Ahammed, M. Akteruzzaman, M. H. Dipu, M. Humayet Islam, M. Ali Hossain and M. Masum Billah, MXene-enhanced perovskite solar cells: Unveiling the superior performance of Mo2TiC2 as an advanced electron transport layer, *Mater. Sci. Eng., B*, 2026, **325**, 119077, DOI: 10.1016/j.mseb.2025.119077.

65 J. Chen and N. Park, Causes and solutions of recombination in perovskite solar cells, *Adv. Mater.*, 2019, **31**, 1803019.

66 S. T. Jan and M. Noman, Influence of layer thickness, defect density, doping concentration, interface defects, work function, working temperature and reflecting coating on lead-free perovskite solar cell, *Sol. Energy*, 2022, **237**, 29–43.

67 B. Mulyanti, M. R. Anwar, C. Wulandari, L. Hasanah, R. E. Pawinanto, I. Hamidah and A. Rusydi, Light absorption enhancement of perovskite solar cells by a modified anti-reflection layer with corrugated void-like nanostructure using finite difference time domain methods, *Phys. Scr.*, 2023, **98**, 65702.

68 A. I. Shimul, A. Ghosh, M. A. Bappy, M. B. Islam, S. O. Aljazzar, J. Y. Al-Humaidi and Y. E. Mukhrish, Numerical insights into CsSnBr3 perovskite solar cells: Evaluating organic charge transport layers using DFT, SCAPS-1D, and wxAMPS simulations, *Opt. Commun.*, 2025, **579**, 131558, DOI: 10.1016/j.optcom.2025.131558.

69 A. Mortadi, E. El Hafidi, M. Monkade and R. El Moznine, Investigating the influence of absorber layer thickness on the performance of perovskite solar cells: a combined simulation and impedance spectroscopy study, *Mater. Sci. Energy Technol.*, 2024, **7**, 158–165.

70 S. T. Jan and M. Noman, Influence of absorption, energy band alignment, electric field, recombination, layer thickness, doping concentration, temperature, reflection and defect densities on MAGeI3 perovskite solar cells with Kesterite HTLs, *Phys. Scr.*, 2022, **97**, 125007.

71 D. Luo, R. Su, W. Zhang, Q. Gong and R. Zhu, Minimizing non-radiative recombination losses in perovskite solar cells, *Nat. Rev. Mater.*, 2020, **5**, 44–60.

72 A. I. Shimul, M. A. Khan, A. Rayhan and A. Ghosh, Machine Learning-Based Optimization and Performance Enhancement of CH3NH3SnBr3 Perovskite Solar Cells with Different Charge Transport Materials Using SCAPS-1D and wxAMPS, *Adv. Theory Simul.*, 2025, **8**, 2500182, DOI: 10.1002/adts.202500182.

73 L. Cao, S.-M. Gu, B. Liu, L. Huang, J. Zhang, Y. Zhu and J. Wang, Highly Ambient Stable $CsSnBr_3$ Perovskite via a New Facile Room-Temperature ''Coprecipitation'' Strategy, *ACS Appl. Mater. Interfaces*, 2023, **15**, 30409–30416, DOI: 10.1021/acsami.3c02532.

74 A.-W. Wang, L.-P. Zhu, Y.-S. Shan, P. Liu, X.-L. Cao and B.-Q. Cao, School of Material Science and Engineering, University of Jinan, Jinan 250022, China, Nuchip Photoelectric Technology Co., Ltd, Zaozhuang 277299, China, High-performance $CsSnBr_3$/Si PN heterojunction photodetectors prepared by pulsed laser deposition epitaxy, *Acta Phys. Sin.*, 2024, **73**, 058503, DOI: 10.7498/aps.73.20231645.

75 A. I. Shimul, A. T. M. S. Islam, A. Ghosh, M. M. Hossain, S. A. Dipa and R. J. Ramalingam, Investigating charge transport layer flexibility for boosted performance in Lead-Free CsSnBr3-based perovskite solar cells, *Comput. Mater. Sci.*, 2025, **250**, 113701, DOI: 10.1016/j.commatsci.2025.113701.

76 M. A. Monnaf, A. Ghosh, A. I. Shimul, Q. Hossain, L. Ferdoush, M. F. I. Buian, A. K. Roy, S. Ahmed,

M. M. Rahman, N. L. Dey, A. R. Chaudhry and M. Al Imran, Numerical Modeling and Machine Learning-Assisted Analysis of Ultra-Thin CuSbS2 Solar Cells Incorporating SnS2 ETL and V2O5 BSF Layers, *J. Inorg. Organomet. Polym.*, 2026, **36**, 1050–1071, DOI: 10.1007/s10904-025-03969-0.

77 T. Nasrin, M. Mottakin, V. Selvanathan, M. I. Hossain, M. Shahiduzzaman, M. A. Islam, M. S. Ahamed, H. F. Alharbi and M. Akhtaruzzaman, Performance optimization and defect studies of Pb-free CsSnBr3-based perovskite solar cells, *Mater. Today Commun.*, 2023, **37**, 107000, DOI: 10.1016/j.mtcomm.2023.107000.

78 A. I. Shimul, A. T. M. S. Islam, A. Ghosh, M. M. Hossain, S. A. Dipa and R. J. Ramalingam, Investigating charge transport layer flexibility for boosted performance in Lead-Free CsSnBr3-based perovskite solar cells, *Comput. Mater. Sci.*, 2025, **250**, 113701, DOI: 10.1016/j.commatsci.2025.113701.

79 S. A. Dar and B. S. Sengar, Analysis of lead free $CsSnBr_3$ based perovskite solar cells utilizing numerical modeling, *Phys. Scr.*, 2024, **99**, 065013, DOI: 10.1088/1402-4896/ad43c7.

80 M. T. Alemu, D. F. Hirpa, K. O. Obodo and C. A. Geffe, Computational investigation of Sb-doped $CsSnBr_3$: insights into structural, electronic, optical, and photovoltaic performance analysis, *Phys. Scr.*, 2025, **100**, 075979, DOI: 10.1088/1402-4896/ade748.

81 S. A. Dar and B. S. Sengar, Optimization and Performance Analysis of Inorganic Lead-Free $CsSnBr_3$ Perovskite Solar Cells Using Diverse Electron Transport Materials, *Energy Fuels*, 2024, **38**, 8229–8248, DOI: 10.1021/acs.energyfuels.4c00953.

82 D. Fang, Y. Tong, F. Xu, B. Mi, D. Cao and Z. Gao, Preparation of CsSnBr3 perovskite film and its all-inorganic solar cells with planar heterojunction, *J. Solid State Chem.*, 2021, **294**, 121902, DOI: 10.1016/j.jssc.2020.121902.

83 S. Gupta, T. Bendikov, G. Hodes and D. Cahen, CsSnBr3, A Lead-Free Halide Perovskite for Long-Term Solar Cell Application: Insights on SnF_2 Addition, *ACS Energy Lett.*, 2016, **1**, 1028–1033, DOI: 10.1021/acsenergylett.6b00402.

84 L.-J. Chen, C.-R. Lee, Y.-J. Chuang, Z.-H. Wu and C. Chen, Synthesis and Optical Properties of Lead-Free Cesium Tin Halide Perovskite Quantum Rods with High-Performance Solar Cell Application, *J. Phys. Chem. Lett.*, 2016, **7**, 5028–5035, DOI: 10.1021/acs.jpclett.6b02344.

85 P. Caprioglio, M. Stolterfoht, C. M. Wolff, T. Unold, B. Rech, S. Albrecht and D. Neher, On the Relation between the Open-Circuit Voltage and Quasi-Fermi Level Splitting in Efficient Perovskite Solar Cells, *Adv. Energy Mater.*, 2019, **9**, 1901631, DOI: 10.1002/aenm.201901631.

86 W. Li, T. Liu, G. Chen, N. Li, X. Wang, Z. Liu and B. Cao, Dual efficacy of potassium-doping in perovskite solar cells: Reducing hysteresis and boosting open-circuit voltage, *J. Appl. Phys.*, 2024, **136**, 165702, DOI: 10.1063/5.0228415.

87 A. Sato, S. Yamaguchi, A. Hasegawa, Y. Shimoi, T. Nakamura, A. Wakamiya and K. Marumoto, Electron diffusion at Sn perovskite/fullerene derivative interfaces and its influence on open-circuit voltage, *npj Flex. Electron.*, 2025, **9**, 47, DOI: 10.1038/s41528-025-00424-5.